International Journal of Biological Macromolecules 380 (2026) 154090

Contents lists available at ScienceDirect

International Journal of Biological Macromolecules

journal homepage: www.elsevier.com/locate/ijbiomac

Structural bases of the conformational transitions of the mitochondrial choline carrier SLC25A48 captured by molecular dynamics simulations

Virginia Quadrotta [a,1], Beatrice Gasperini [a,1], Andrea Pasquadibisceglie [b,*], Fabio Polticelli [a,c,**]

[a] Department of Science, University Roma Tre, Viale G. Marconi 446, 00146 Rome, Italy
[b] Telethon Institute of Genetics and Medicine (TIGEM), Pozzuoli, 80078, Italy
[c] National Institute of Nuclear Physics, Roma Tre Section, Via della Vasca Navale 84, 00146, Roma, Italy

ARTICLE INFO

Keywords:
Mitochondrial carrier
SLC25
Conformational transitions
SLC25A48
Mitochondrial choline carrier
Molecular dynamics simulations
Gating mechanism
M2 loop

ABSTRACT

The mitochondrial choline carrier SLC25A48 mediates choline import into the mitochondrial matrix, supporting one-carbon metabolism and epigenetic regulation. Despite its physiological relevance, the structural determinants of substrate recognition and conformational transitions remain poorly characterized.

Here, the conformational dynamics of human SLC25A48 was investigated using deep-learning-based structure prediction combined with multiple extensive molecular dynamics simulations in a realistic mitochondrial membrane environment. Structural models representing the cytoplasmic-open (c-state), occluded and matrix-open (m-state) conformations were generated and used as starting points for MD simulations, for a total of 21 μs.

Unbiased simulations captured spontaneous, bidirectional transitions between the occluded and m-state, confirmed by structural convergence and comparison with available crystal structures, and shown to remain well separated in a distinct descriptor space by a supervised classifier (LDA). Transitions were driven by an asymmetric rearrangement primarily involving Domain I, while the remaining helices behaved as a rigid scaffold, consistent with mechanistic features described for other SLC25 carriers. A matrix-side loop, whose dynamics correlated with this asymmetry, adopted distinct capping and opening conformations across states, suggesting a complementary gating role. Choline remained stably coordinated throughout the transition, indicating that the conformational change corresponds to the opening step of the transport cycle rather than substrate release. Context-dependent lipid interactions were also observed, affecting ligand position or carrier conformation.

These results provide mechanistic insight into SLC25A48 conformational plasticity and a structural framework, with candidate collective variables, to guide future investigation of mitochondrial choline transport.

1. Introduction

Metabolic homeostasis relies on membrane transport proteins that regulate the exchange of ions and metabolites across biological membranes. Within mitochondria, the Solute Carrier Family 25 (SLC25) mediates the selective transport of a wide variety of molecules across the inner mitochondrial membrane (IMM), thereby contributing to metabolic flux control, energy balance and signaling regulation [1].

Among its members, SLC25A48 has been recently identified as a high-affinity mitochondrial choline transporter [2–4]. In detail, SLC25A48 mediates the transport of choline into the mitochondrial matrix, sustaining its conversion to betaine, a methyl donor crucial for epigenetic regulation and methionine biosynthesis. Choline is also a component of cell membrane lipids, such as phosphatidylcholine, and is involved in the production of acetylcholine and one-carbon metabolism [5,6]. Despite its relevance in cell physiology, the structural determinants responsible for choline recognition and translocation remain poorly defined, and the molecular mechanisms governing transport are still largely uncharacterized.

From a structural viewpoint, the members of the SLC25 family are formed by a three-fold repeat organization. Each repeat corresponds to a homologous domain composed of an odd-numbered transmembrane

* Correspondene to: A. Pasquadibisceglie, Telethon Institute of Genetics and Medicine (TIGEM), Via Campi Flegrei, 34, 80078, Pozzuoli, Italy.
** Correspondene to: F. Polticelli, Department of Science, Roma Tre University, Viale G. Marconi 446, 00146, Rome, Italy.
E-mail addresses: virginia.quadrotta@uniroma3.it (V. Quadrotta), beatrice.gasperini@uniroma3.it (B. Gasperini), a.pasquadibisceglie@tigem.it (A. Pasquadibisceglie), fabio.polticelli@uniroma3.it (F. Polticelli).
[1] These two authors contributed equally to this work.

https://doi.org/10.1016/j.ijbiomac.2026.154090
Received 18 December 2025; Received in revised form 13 August 2026; Accepted 14 August 2026
Available online 17 August 2026
0141-8130/© 2026 The Authors. Published by Elsevier B.V. This is an open access article under the CC BY license (http://creativecommons.org/licenses/by/4.0/).

(TM) α-helix followed by a short α-helix, exposed on the mitochondrial matrix side, and an even-numbered TM α-helix, in the sequential arrangement H1-h12-H2 (Domain I), H3-h34-H4 (Domain II) and H5-h56-H6 (Domain III) (Fig. 1). SLC25 proteins cycle between two states, conventionally called the cytoplasmic (c-) and matrix (m-) state, in which the substrate binding site is transiently accessible either to the intermembrane space (IMS) or to the matrix, allowing selective import or export of ligands. In this type of transport mechanism, called alternating access, the transition between c- and m-state involves an occluded state in which the substrate is inaccessible from both sides of the membrane. Residues belonging to a conserved sequence signature motif, PX[DE]XX[KR], located in the even-numbered α-helices, form a salt bridges network in the c-state, which closes the transporter on the matrix side (m-network). Residues from a less conserved motif, *i.e.*, [FY][DE]XX[KR], stabilize in a similar manner the transporter in the m-state conformation (c-network). In conjunction with the charged residues of the c-network, a layer of aromatic and aliphatic residues, called the hydrophobic plug, contributes to further stabilization of the m-state conformation and prevents proton leakage across the IMM (Fig. 1) [7].

While the alternating access is the widely accepted mechanistic hypothesis for SLC25 transporters, the precise determinants guiding the conformational cycle and the contribution of individual structural elements remain unclear.

In the present work, the conformational dynamics of SLC25A48 has been investigated using deep learning derived structural models and extensive atomistic molecular dynamics (MD) simulations, under conditions mimicking the physiological IMM environment. The stability of the c-, occluded and m-states was analyzed, providing a framework to understand how structural elements govern substrate recognition and conformational transitions. Taken together, these results provide new structural insights into SLC25A48 ligand binding and conformational transitions and provide the basis for future experimental validation.

2. Methods

2.1. Protein structure prediction

The human SLC25A48 amino acid sequence (UniProt ID: Q6ZT89) [10] has been used to predict the structural models of the transporter in the c-state, m-state and occluded state conformations.

AlphaFold3 [11], developed by Google DeepMind and Isomorphic Labs, has been used with default settings to generate five predictions for the carrier in the c-state apo conformation. The model with the highest confidence score (pLDDT) was chosen as the representative c-state conformation for subsequent analysis. The pLDDT score is a confidence metric that ranges from 0 to 100: values higher than 90 indicate regions with high confidence in both the backbone and side chains; scores between 90 and 70 usually correspond to a correct backbone positioning with misplacement of some side chains, while scores ranging from 50 to 70 reflect low confidence.

To obtain the structural model of the transporter in the m-state conformation, the Colab Notebook "ColabFold v1.5.5: AlphaFold2 using MMseqs2" has been used (https://colab.research.google.com/github/sokrypton/ColabFold/blob/main/beta/AlphaFold2_advanced.ipynb) [12]. The predictions were performed using the following parameters: max_msa_clusters = 32, specifying the number of sequence clusters randomly selected for input to the AF2 neural network, and max_extra_msa = 64, defining the number of additional sequences used to compute supplementary summary statistics. MSA depth was intentionally restricted, resulting in stochastic subsampling of homologous sequences and attenuation of co-evolutionary constraints that typically bias AlphaFold toward the dominant conformational state. It should be noted that the ideal values for these settings may vary depending on the particular protein under study.

The TM-Align algorithm [13] has then been applied on the 40 structures modelled by ColabFold to identify the best representative m-state structural model, by comparing them with the only known crystal structure of a mitochondrial carrier in the m-state conformation, *i.e.* the fungal AAC from *Thermothelomyces thermophila* (PDB ID: 6GCI) [9].

The model presenting the highest TM-score, *i.e.*, the best match for the m-state conformation, was selected for subsequent analyses.

The occluded conformation of the carrier has been obtained using Boltz-1 [14], an open-source deep learning model reported to achieve accuracy comparable to AlphaFold3 on standard benchmarks. Both the apo and choline-bound proteins have been obtained using default configuration options, and the models with the highest confidence score

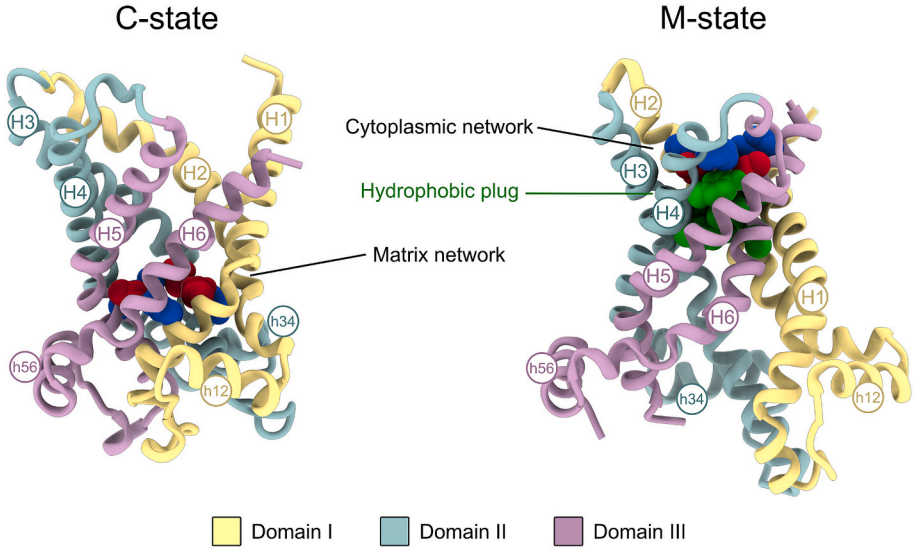

Fig. 1. Structural motifs of SLC25 carriers. Schematic view of the c-state and m-state crystallographic structures of the ADP/ATP carrier (AAC, SLC25A4). This is the most extensively studied member of the SLC25 family and currently the only one for which the structure of both conformational states has been determined experimentally. Cytoplasmic and matrix network residues are shown as van der Waals spheres and colored in red (negatively charged) or blue (positively charged). Hydrophobic plug residues are shown as van der Waals spheres and colored in green. The c-state shown here corresponds to the bovine AAC from *Bos taurus* (PDB ID: 1OKC) [8], while the m-state corresponds to the fungal AAC from *Thermothelomyces thermophila* (PDB ID: 6GCI) [9]. Missing regions, such as terminal segments and inter-helical loops, are not shown because they are unresolved in the crystallographic structures.

were selected.

The models described above were used as starting structures to build the simulation boxes for the MD simulations as reported in the following section. Additional structural models generated for comparison purposes are described in the *Supplementary Methods Section 1*.

2.2. MD simulations of the SLC25A48 conformations

Each SLC25A48 model was embedded in an IMM bilayer generated through CHARMM-GUI (http://www.charmm-gui.org, accessed on 15 July 2025) [15–17]. The membrane composition was based on the IMM model published by the CHARMM-GUI team, available at the CHARMM-GUI Archive [18]; minor modifications were applied to better reflect leaflet asymmetry. Two 22.5 Å-thick layers of TIP3P water molecules were placed above and below the membrane, and Na^+ and Cl^- ions were added to neutralize the system and achieve 0.15 M ionic strength. System dimensions and full compositional details (box size, lipid, water and ion content) are reported for each state in Table S1 and S2. The starting coordinate files for all simulation boxes are deposited on Zenodo (https://doi.org/10.5281/zenodo.21721870), allowing direct inspection of the complete computational setup.

MD simulations were performed using the CHARMM36m force field [19] in combination with the AMBER24 software [20], using periodic boundary conditions with box geometry and protein-to-edge distance following default CHARMM-GUI settings for membrane systems. Initial energy minimization was carried out with positional restraints on the protein (10 kcal mol^{-1} $Å^{-2}$) and membrane (2.5 kcal mol^{-1} $Å^{-2}$), using 2500 steps of steepest descent followed by 2500 steps of conjugate gradient to relax unfavorable contacts. After minimization, the system was gradually heated to 310.15 K under the NVT ensemble, followed by NPT equilibration to stabilize pressure at 1 bar. Throughout these thermalization and pressure equilibration phases, the force constants of the positional restraints were progressively weakened. Finally, the equilibrated systems were properly simulated without restraints using the NPT ensemble for a total of 1 μs, in replica. The same protocol was applied to protein-ligand complexes. During equilibration, choline was restrained as if it were a protein residue, with the same force constants progressively released across the equilibration stages. Simulations were carried out with periodic boundary conditions and a 2 fs integration step; temperature was controlled using a Langevin thermostat, while semi-isotropic pressure was maintained *via* a Monte Carlo barostat at 1 bar [21]. Long-range electrostatics were computed using Particle Mesh Ewald (PME) [22] with a 12 Å cutoff and a force-switching function starting at 10 Å.

All the methodological details of the analyses performed on the MD trajectories, such as protein interactions, RMSF, radius of gyration, membrane curvature, principal component analysis and clustering of representative conformations, are reported in the *Supplementary Methods Section 2*. Where applicable, values are reported in the text as mean ± standard error of the mean (SEM) across independent replicas. Standard deviation (SD) is used instead when reporting the dispersion of frame-level quantities within a single trajectory or pooled dataset, where frames are not statistically independent.

2.3. Molecular docking

To generate the c-state complex with choline (holo form), docking simulations were performed using GNINA, a Smina derivative [23] that couples classical scoring with a convolutional neural network (CNN) module [24]. Choline was retrieved from the ZINC15 database [25] and docked into the c-state model within a 20.25 × 22.5 × 26.29 Å search box centered on the translocation cavity, with sampling exhaustiveness raised to 64 to ensure broad coverage of the binding-poses landscape. Different combinations of GNINA's scoring options were screened (Table S3), and *–scoring* vina with *–cnn_scoring* rescore was retained as it produced poses combining the most favorable predicted affinity and the highest CNN confidence. Indeed, GNINA returns two complementary scores: the minimized affinity, comparable to standard docking energies, and the CNN score (0–1 scale), which expresses the agreement of the pose with learned binding patterns without a direct energetic interpretation. The retained poses were inspected manually in Chimera and ChimeraX [26,27] to verify reasonable orientations and interactions.

2.4. Density-based clustering of conformational states

Density-based conformational landscape clustering using InfleCS [28] was applied to the MD trajectories to identify kinetic metastable states, in the space defined by two collective variables: the mass-weighted radius of gyration of the m-network (Cα atoms of residues Asp27, Lys30, Asp125, Lys128, Asp238, Lys241, forming the salt-bridges network) and of the hydrophobic plug (Cα atoms of residues Val76, Phe77, Phe80, Tyr195, Phe196, Tyr199, Met291, Phe292, Tyr295). Frames from all the trajectories were decorrelated per replica using autocorrelation-time-based subsampling (62–250 ns lag, replica-specific), yielding 141 statistically independent frames. InfleCS identified four core density basins corresponding to the abortive c-state, c-state, occluded and m-state conformations. The fitted density model was then applied to a denser subsampling of all 21 trajectories at fixed 1-ns intervals (21,000 frames total) to assign a conformational label to each frame. Frames whose collective-variable coordinates fell outside all four core density regions (12,591 of 21,000) were classified as transition points and excluded from the primary dataset (retained frames: 8409).

To determine whether the intraprotein distances that best discriminate between the four states provide a distinct structural signature of these populations, a Linear Discriminant Analysis (LDA) was trained on the labeled frames and further tested on the excluded transition-point frames; full methodological details are provided in the *Supplementary Methods Section 3*.

3. Results and discussion

In this study, the three main conformational states of the human mitochondrial carrier SLC25A48 were modelled using deep learning approaches; namely the c-state, m-state, and, for the first time for a SLC25 member, the occluded state.

The c- and occluded (o-) state were modelled both in the presence and absence of the endogenous substrate choline (i.e., holo and apo forms). SLC25A48 is known to mediate choline import into mitochondria [2–4], however, whether it also exports any substrate remains unknown; therefore, the m-state conformation was modelled only in the apo form.

These five apo and holo representative models were used as starting points for all-atom MD simulations, to investigate the conformational landscape of the transporter. Five independent replicas, each lasting 1 μs, were performed for each starting conformation. In the case of the c-state system, three apo replicas were performed from the predicted model and three holo replicas starting from the choline docking complex. Altogether, the MD simulations covered a total of 21 μs, representing a substantial sampling of the protein's conformational space.

3.1. Deep learning based modelling of SLC25A48

AlphaFold3 (AF3, https://alphafoldserver.com) [11] was used to model the three-dimensional structure of the human mitochondrial carrier SLC25A48. The predicted structural model with the highest confidence score (pLDDT = 73.68, Fig. 2) displayed a conformation open toward the IMS and a closed matrix side, consistent with the canonical features of the c-state, resembling the conformation of other SLC25 carriers like AAC (PDB ID: 1OKC [8]) and UCP1 (SLC25A7, PDB ID: 8HBV [29]). The model also displayed a pTM of 0.74, a global estimate of the predicted structural accuracy of the fold, complementing the per-residue or (per-atom) confidence given by pLDDT. The use of

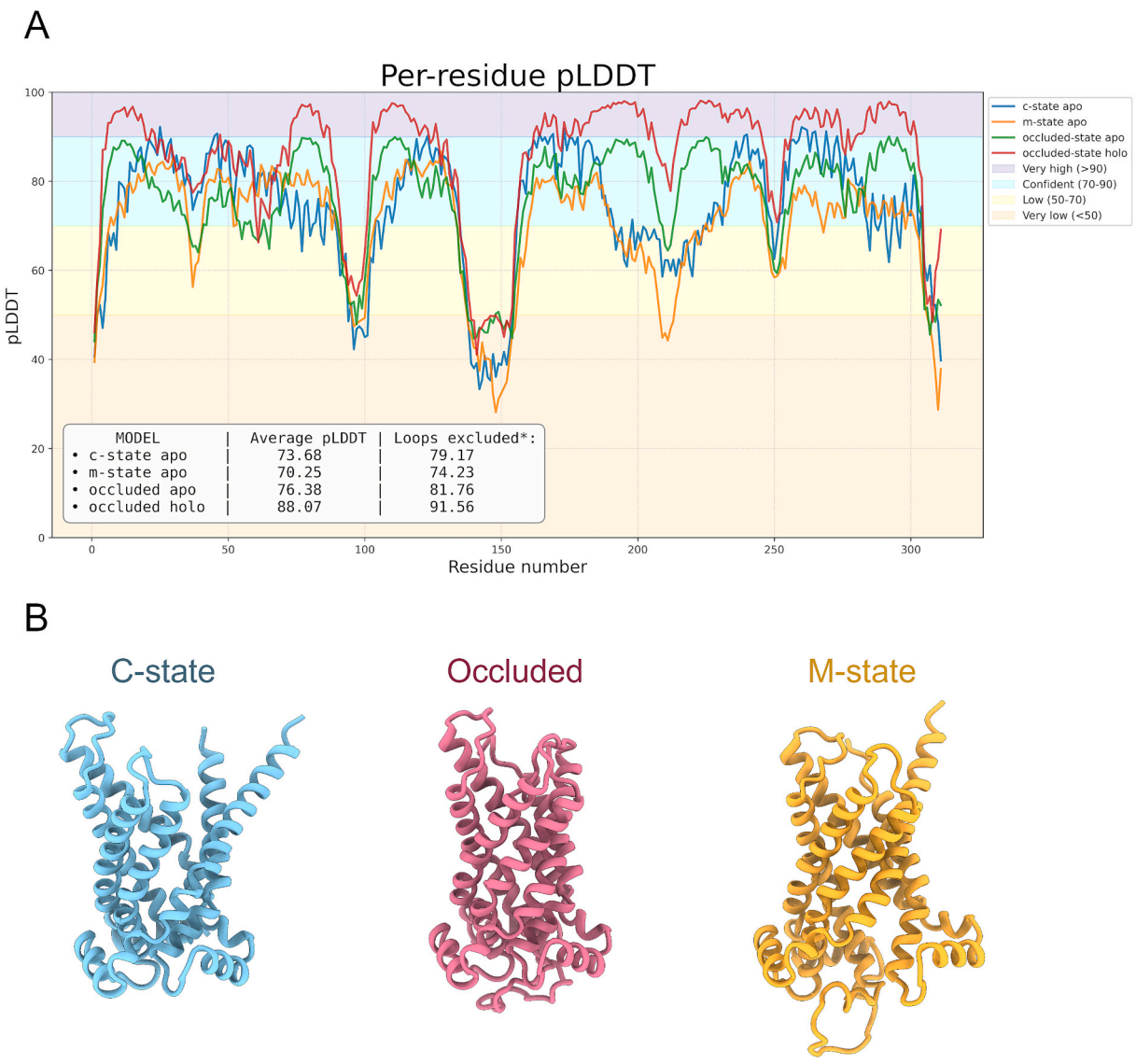

Fig. 2. (A) Per-residue pLDDT score of the predicted models. As described in the text the average pLDDT has also been recalculated excluding loops and terminal regions. The regions excluded (*) were 1–5, 36–41, 91–103, 133–159, 205–216, 247–255 and 307–311. The graph also shows horizontal confidence bands, detailed in the legend. (B) From left to right: the c-state model predicted by AF3, the occluded model predicted by Boltz-1 and the m-state model obtained with ColabFold.

pLDDT as a local confidence metric is well-supported by extensive benchmarks showing a strong correlation between high scores and low Cα root-mean-square error relative to experimental structures [30,31]. It is important to note that SLC25A48 displays several disordered loops on both the IMS and matrix sides, and it has been demonstrated that very low pLDDT scores correlate with high propensities for highly flexible or intrinsically disordered regions (IDR) [31,32]. For this reason, the average confidence score has been recalculated by removing loop regions: in detail, the regions excluded were the first and last five residues (1–5 and 307–311), the two IMS loops that connect H2 to H3 and H4 to H5 (91–103 and 205–216) and the three matrix loops that connect the odd-numbered helix of each domain to the following matrix helix (36–41, 133–159 and 247–255). By doing so, the average pLDDT score of the c-state increased from 73.68 to 79.17.

To further validate this fold, the c-state model was compared to the crystallographic structure of the bovine AAC (PDB ID: 1OKC [8]) using TM-align [13], an algorithm for sequence independent protein structure comparisons. TM-align yields a TM-score between 0 and 1; values below 0.2 are typical of unrelated proteins, while values above 0.5 generally indicate the same fold [13]. In this case the resulting score was 0.81, despite only approximately 20% sequence identity between the proteins, reinforcing the reliability of the predicted model.

Structural convergence was additionally confirmed by low RMSD values calculated for the m-network residues (Table 1), a key hallmark and accepted metric of c-state formation. A superimposition between the three domains of the c-state model and the bovine protein crystallographic structure, as well as the superimposition of the residues of the m-

Table 1
RMSD values for the m-network residues in SLC25A48 predicted models used as starting points for MD simulations, relative to the bovine SLC25A4 (AAC) c-state crystallographic structure (PDB ID: 1OKC).

M-network residues	RMSD (Å)		
SLC25A48 - SLC25A4	c-state	o-holo	o-apo
D27 - E29	1.06	1.07	1.34
K30 - K32	0.46	0.51	1.01
D125 - D134	1.15	1.04	1.16
K128 - R137	0.85	0.78	0.71
D238 - D231	1.13	1.51	1.06
K241 - R234	1.18	1.39	0.97

network, is shown in Supplementary Fig. S1.

To model the transporter in the m-state conformation, ColabFold with advanced settings was employed, using reduced MSA depth resulting in stochastic subsampling of homologous sequences [12,33]. Limiting MSA depth attenuates co-evolutionary coupling signals that typically bias AlphaFold2 toward the dominant conformational state. As previously observed in studies leveraging AlphaFold2 for conformational sampling, residue pairs stabilizing distinct functional states may co-evolve across homologs; therefore, deep MSAs tend to reinforce a single prevalent structural solution, whereas MSA depth reduction can partially relax these constraints and enable the emergence of alternative conformations [33]. While this stochastic approach has proven to be effective for capturing alternative states in various transporters [33–35], it is important to acknowledge its limitations, as it relies on stochastic attenuation of co-evolutionary signals that stabilize the dominant fold [36].

To overcome these hurdles, recent advancements have introduced more controlled methodologies; these include the use of pre-defined collective variables or biased structural templates to steer the prediction toward specific functional states, as well as approaches based on local frustration analysis, which identify metamorphic regions prone to structural transitions [36–40].

In the present study, to ensure the physical relevance of the model obtained, the representative m-state model was selected as the structure displaying the highest structural similarity to the only known crystal structure of a mitochondrial carrier in the m-state conformation, *i.e.* the fungal AAC from *Thermothelomyces thermophila* (PDB ID: 6GCI) [9].

The structural similarity has again been evaluated using TM-align, and in this case, the selected model displayed a TM-score of 0.75 and an initial pLDDT score of 70.25, increased to 74.23 after accounting for disordered regions. Snapshots showing a superimposition between the predicted model and the experimental structure are provided in Fig. S2.

Consistent with a matrix-open state, the model featured a sealed hydrophobic plug. On the other hand, SLC25A48 lacks a canonical [FY][DE]XX[KR] motif, resulting in the absence of a canonical salt-bridges c-network. As previously noted, these motifs are significantly less conserved across the SLC25 family compared to those forming the m-network and frequently form incomplete networks or are entirely absent [41,42]. For this reason, the residues of the conserved hydrophobic plug, fundamental for preventing proton leakage in the m-state, have been compared to those of the crystal structure. Again, the low RMSD values obtained further support the reliability of the selected m-state model (Table 2).

Finally, Boltz-1 [14] was employed primarily to allow the prediction of the SLC25A48-choline complex, a ligand not currently supported by AlphaFold3 webserver. Upon observing that Boltz-1 naturally favored an occluded state for the holo-complex, its use has been extended to the apo-form to allow for a direct comparison of the occluded states.

In both cases, all the predicted models displayed high confidence scores and exhibited closure on both sides of the membrane, as expected for an occluded conformation.

The top ranks displayed average initial pLDDT scores of 76.38 for the apo and 88.07 for the holo-form, which increased to 81.76 and 91.56 when excluding IDRs (pTM = 0.68 and 0.87, respectively). Notably for the holo conformation the ipTM, which measures the accuracy of the predicted interface within a protein-ligand complex, was also very high (0.93).

In the case of the occluded conformations, given that they simultaneously display a closed m-network and a sealed hydrophobic plug, the RMSD between the aforementioned residues was calculated and values are included in both Table 1 and Table 2. In addition, a superimposition of the m-network and the hydrophobic plug residues of the occluded models and the crystal structures is shown in Fig. S3.

To evaluate the potential influence of the lipid environment on the predicted conformation, an additional model was generated using Boltz-1, including choline and 23 lipid molecules, mimicking the IMM (*Supplementary Methods Section 1*). This approach was inspired by the CoMPLip strategy [43], which demonstrates that co-folding membrane proteins with explicit lipid molecules during structure prediction imposes a membrane-like context and can improve structural accuracy and conformational state sampling. The resulting model preserves the occluded conformation (Fig. S4) and displays a mean pLDDT of 81.98, increased to 89.66 after exclusion of loop regions.

To further investigate whether independent prediction methods converge toward a consistent conformational state of SLC25A48, an additional structure prediction was performed using ESMFold [44], a method not related to the AF3/Boltz-1 framework. The resulting model displays high confidence (pLDDT = 88.19 and pTM = 0.92) and, surprisingly, also adopts an occluded conformation, even though no experimental structure is available in this state for any member of the SLC25 family, which limits the risk of template-driven bias. Notably, the transmembrane core is highly consistent with the Boltz-1 models, with minor differences limited only to flexible loop regions and terminal segments (Fig. S5).

Taken together, the high structural similarity with the experimental templates, the consistent pLDDT scores and the stabilization of the key gating elements confirm the reliability of the predicted models. Notably, the occluded holo state displays the highest confidence value (pLDDT >90), suggesting that the presence of the substrate further increases the reliability of the predicted transporter's architecture and providing a robust foundation for subsequent MD simulations.

Table 2
RMSD values for the hydrophobic plug residues in SLC25A48 predicted models used as starting points for MD simulations, relative to the fungal SLC25A4 (AAC) m-state crystallographic structure (PDB ID: 6GCI). Residues absent in the crystallographic structure (*i.e.*, not conserved) are indicated with "\".

Hydrophobic plug residues	RMSD (Å)		
SLC25A48 - SLC25A4	m-state	o-holo	o-apo
V76 - \	\	\	\
F77 - F97	1.56	0.84	1.27
F80 -	\	\	
Y195 - Y200	1.03	0.74	0.65
F196 - F201	1.98	1.10	0.83
Y199 - Y204	0.74	0.92	1.19
M291 - V294	1.17	1.44	1.86
F292 - L295	2.07	1.34	1.66
Y295 - Y298	1.39	1.95	2.6

3.2. Conformational dynamics of SLC25A48

3.2.1. Spontaneous transitions validate SLC25A48 occluded model

The strongest validation for the proposed models is the occurrence of spontaneous conformational transitions in opposite directions during unbiased MD simulations. Among the 21 independent simulations, the five initiated in the occluded state (four in the presence and one in the absence of choline) spontaneously evolved toward an m-state conformation. Specifically, the first replica of the apo system (*o-apo 1*) and all holo simulations except the second (*o-holo 1, 3, 4 and 5*) underwent large-scale rearrangements, reaching an architecture corresponding to a sealed hydrophobic plug and an open m-network, consistent with the canonical m-state of SLC25 proteins. Conversely, among the five m-state simulations, the transporter remained in the starting conformation in four (*m-apo 2–5*), while the first replica (*m-apo 1*) sampled a reverse transition back toward the occluded state.

To confirm the physical plausibility of these simulations, the stability of the hydrophobic plug, physiologically required to prevent proton leakage when the protein is open toward the matrix side [7], was evaluated through the RMSF of its residues (Table S4). Values were lower than 1 Å and comparable across all groups regardless of transition: 0.67 ± 0.02 Å in the stably occluded replicas (mean ± SEM, $N = 5$), 0.72 ± 0.05 Å in the four native m-state replicas and 0.73 ± 0.05 Å in the five

o-to-m transitioning replicas. The reverse m-to-o transition (*m-apo 1*) gave a comparable low value of 0.76 Å. This consistency confirms that the hydrophobic plug is a conserved, stably packed gating element, independent of transition status (Fig. S6).

Additionally, the extent of conformational opening during the transitions was quantified by calculating the radius of gyration (Rg) on selected groups of residues. The first two groups represent the m-network and the hydrophobic plug: the two structural elements whose closure/opening defines the gating state of the transporter (Fig. 3). The others are two additional "rings" of residues, chosen to capture the extent of opening at different heights along the membrane normal: a c-side (top) ring positioned below the hydrophobic plug (Gly16, Asn73, Gly114, Tyr192, Gly227, Ser288) and a matrix ring formed by residues belonging to the matrix helices (Arg47, Thr166, Ser262). The plug and top rings remained remarkably stable across all simulations, consistent with persistent c-side sealing. The m-network and matrix ring instead increased markedly in systems sampling opening, with *o-holo 1* showing the largest increase; while *m-apo 1* displayed a progressive decrease consistent with its closure, reaching values comparable to the non-transitioning replicas shown as controls.

A distinct case is represented by *o-holo 2*, a replica that exhibited a behavior different from its sister o-holo simulations. Indeed, this replica initially followed the same opening trend as the others, with partial expansion of the matrix helices, but did not complete the transition since the transmembrane core remained sealed. The resulting ensemble thus represents an intermediate conformation between the occluded and the m-state, recalling the "inward-open partially occluded" conformations described for transporters of the Major Facilitator Superfamily (MFS), such as the xylose transporter XylE from *E. coli* (PDB IDs: 4JA3, 4JA4) [45]. Consistent with this intermediate character, only the matrix ring showed an increase in Rg for *o-holo 2*, while the m-network remained stable at values comparable to the non-transitioning replicas. This observation suggests that additional, partially occluded substates along the transition pathway cannot be excluded.

The geometric picture emerged from the Rg analysis is further corroborated by the overall structural convergence of each trajectory toward its target conformation.

The centroids of the most populated cluster of *m-apo 2* and *o-apo 4*, obtained by RMSD-clustering on the protein backbone (*Supplementary Methods Section 2.3*), were selected as reference structures for the m-state and occluded state, respectively. In detail, *m-apo 2* was chosen for its highest similarity to the experimental m-state crystal structure among the native m-state replicas (TM-score 0.78; Table 3). Since no experimental structure is available for the occluded state, as already noted, *o-apo 4* was instead selected as the most stable among the occluded replicas (Fig. S7).

All transitioning systems displayed a clear and progressive decrease of the RMSD values relative to these reference structures (Fig. 4) and, interestingly, the holo systems reached m-like values within the first 100–150 ns, whereas the apo systems approached the plateau only after around 400 ns, in both directions.

A separate comparison of the *o-holo 2* replica further confirmed its intermediate character: while the TM helices converge toward the occluded reference, the matrix helices diverge substantially, consistent with the partial widening observed (Fig. S8).

As an additional quantitative measure of similarity, backbone RMSD was also calculated between the centroid of the most populated cluster of each transitioning system and the chosen reference. In the case of the o-to-m replicas (*o-apo 1*, *o-holo 1*, *o-holo 3*, *o-holo 4* and *o-holo 5*) low average values (1.631, 1.730, 1.561, 1.757 and 1.401 Å) indicate strong structural overlap, confirming that all simulations converge toward a structurally similar m-state, comparable to the native m-state replica. The reverse m-to-o transition (*m-apo 1*) gave a comparable low value, with a backbone RMSD of only 1.223 Å between its centroid and the occluded reference.

A further, external validation of the sampled conformations was obtained by TM-align, comparing the same centroids of each o-to-m transition or stable m-state simulation against the fungal m-state crystal structure [9], with TM-scores ranging from 0.74 to 0.81 (Table 3). These values indicate a high degree of structural similarity, particularly considering that this global comparison also includes flexible loops and terminal regions that lower the score. Notably, *o-holo 1* showed the highest similarity to the experimental structure; a structural superimposition is shown in Supplementary Fig. S9.

It is important to note that spontaneous transitions might be due to an unstable artificial starting point (*i.e.,* the predicted occluded state could be an artifact) or to a physically relevant process where the occluded metastable state overcomes a low energetic barrier to convert into the m-state. The fact that a spontaneous reverse m-to-o transition (*m-apo 1*) has been observed without the application of external biases, reaching the same occluded state used to start the occluded simulations with a low backbone RMSD (~1 Å, see above), argues strongly against the artifact hypothesis. Moreover, this is further supported by the substrate dependence of the transition: the occluded apo and holo starting models are structurally nearly identical (backbone RMSD 0.489 Å; TM-score 0.98), yet four of five holo replicas left the occluded basin within 150 ns while four of five apo replicas remained occluded for the full microsecond. A starting structure lying on a downhill slope would be

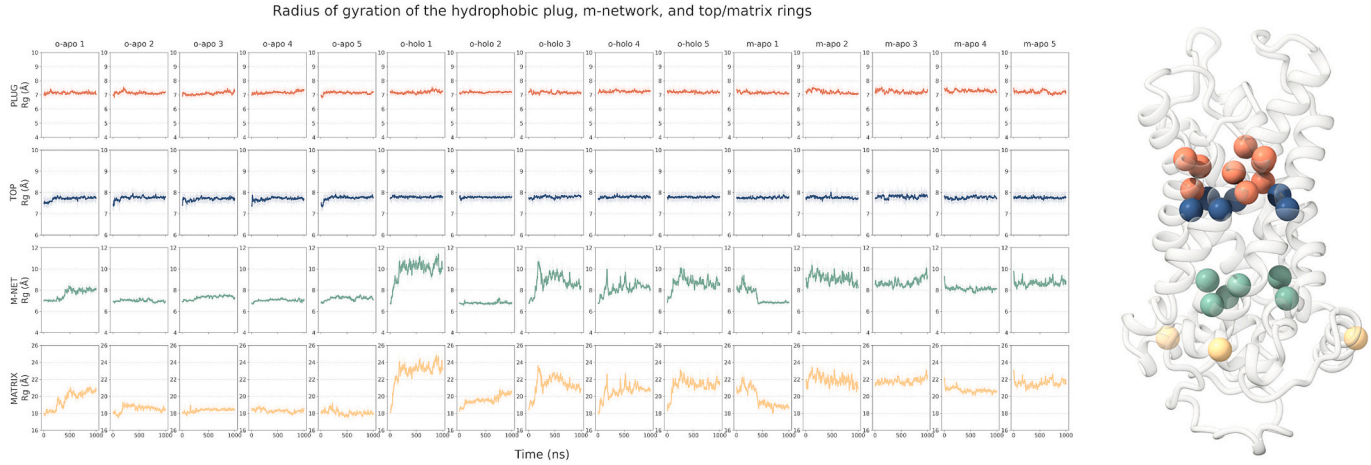

Fig. 3. Radius of gyration (Rg) of the hydrophobic plug, the m-network and two structural rings distributed along the membrane z-axis, shown for each of the 15 occluded and m-state replicas (5 o-apo, 5 o-holo, 5 m-apo). On the right, the structure of the transporter is shown with the Cα atoms of the residues defining each of the four groups displayed as spheres, colored to match the corresponding trace.

Table 3
TM-scores calculated between the centroid of the most populated cluster from each MD simulation that reached or stayed in the m-state conformation and the fungal experimental m-state crystal structure.

System	o-apo 1	o-holo 1	o-holo 3	o-holo 4	o-holo 5	m-apo 2	m-apo 3	m-apo 4	m-apo 5
TM-score	0.74	0.81	0.77	0.74	0.76	0.78	0.76	0.75	0.76

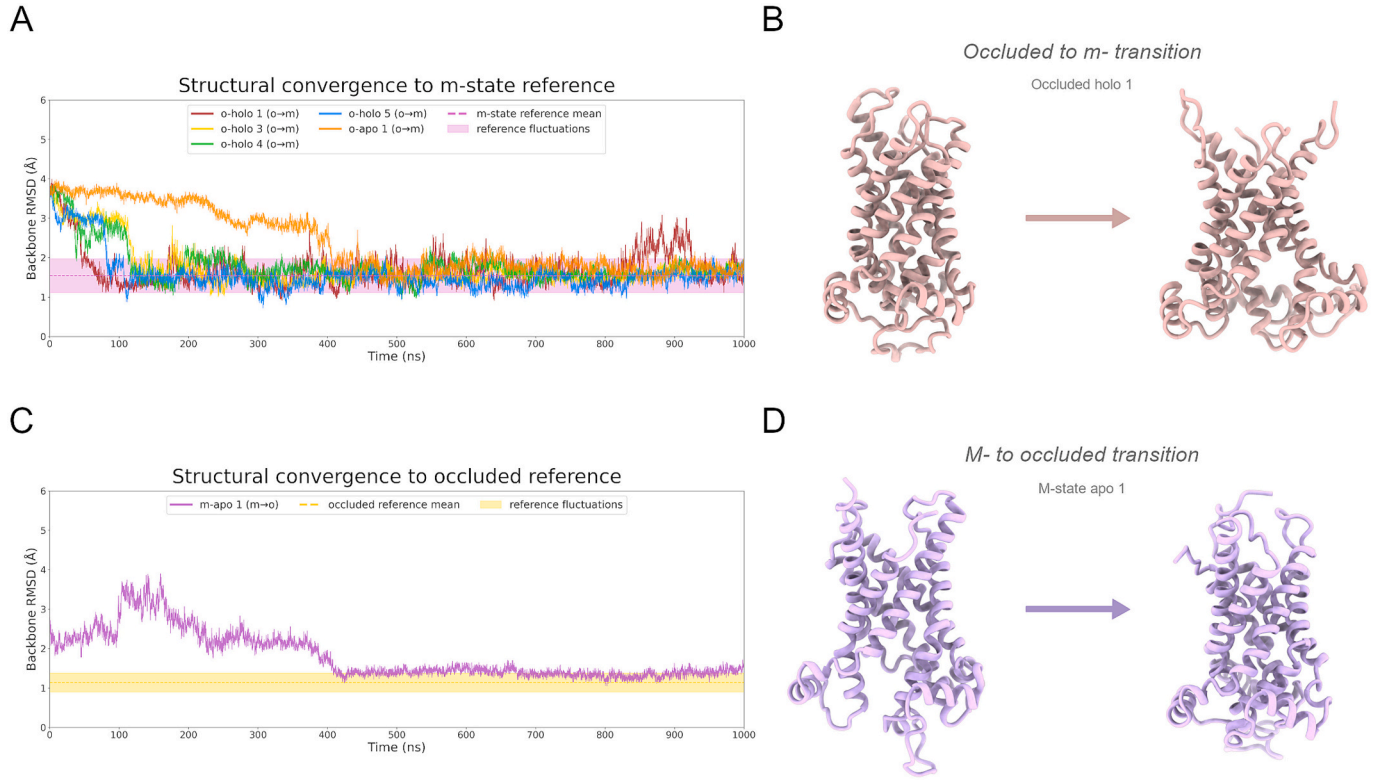

Fig. 4. Structural convergence during the SLC25A48 o-to-m and m-to-o transitions. (A) RMSD of the TM helices relative to the centroid of the most populated cluster of *m-apo 2* (in orchid), used as the m-state reference, for all o-to-m transitioning replicas. (B) Structural representation of an o-to-m transition, illustrated using *o-holo 1* as an example. The starting occluded conformation (left) and the centroid of the most populated cluster (right), which adopted an m-state conformation, are shown to highlight the extent of the opening movement. (C) RMSD of the TM helices relative to the centroid of the most populated cluster of *o-apo 4* (in yellow), used as the occluded reference structure, for the reverse m-to-o transition. The plot shows the convergence of *m-apo 1* (in purple) toward the occluded conformation at around 400 ns. (D) Structural representation of the m-to-o transition, illustrated using *m-apo 1*. The starting m-state structure (left) and the centroid of the most populated cluster (right), which closed into the occluded conformation, are shown to highlight the closure of the matrix side.

expected to relax irrespective of ligand occupancy; such divergent behavior between two systems differing only for the presence of choline is difficult to reconcile with simple relaxation and corresponds instead to what an alternating-access cycle requires, since substrate binding must destabilize the occluded intermediate for turnover to proceed.

The agreement between conformations obtained from independent unbiased simulations starting from different modelled states, and the substrate dependence of the transition, supports the reliability of the initial structural predictions and supports the physical plausibility of the obtained metastable states.

3.2.2. *Kinetic metastable states*

Apart from the replicas that underwent the conformational transitions discussed in Section 3.2.1, most simulations remained in their starting conformation throughout the microsecond timescale, defining kinetically metastable states. To characterize these states, frames from all trajectories were decorrelated as described in the Methods Section 2.4 and projected onto the two collective coordinates introduced above, *i.e.* the Rg of the m-network and hydrophobic plug. This approach was inspired by Pietropaolo and colleagues, who used the Rg of gate regions as collective variables to reconstruct the free-energy landscape of AAC [46]. In the present case, the decorrelated distribution obtained from unbiased sampling was instead clustered using InfleCS [28], a density-based clustering algorithm that leverages Gaussian Mixture Models and the Hessian matrix. By locating density inflection points, InfleCS cleanly isolates stable core states from transition regions in MD trajectories.

InfleCS identified four core populations (Fig. 5, Panel A), corresponding to the m-state, occluded and two c-state subpopulations. Frames classified into the additional c-state population come almost entirely from the early portion of a single replica (*c-apo 1*), which subsequently relaxed toward a likely physiological c-state conformation. This basin is characterized by a markedly more open hydrophobic plug, with a mean Rg of 11.50 ± 0.13 Å compared to 9.66 ± 0.20 Å in the physiological c-state basin. The former population is structurally reminiscent of the "abortive" enlarged conformations described for inhibitor-bound AAC structures [47] and for this reason it has been classified as abortive.

Occupancy analysis confirms that stable replicas occupied almost exclusively their expected basin: the c-apo and c-holo replicas populated the c-state exclusively, with a minor fraction in the abortive subpopulation (8% of the combined c- and abortive population; 95% of which from *c-apo 1*); while non-transitioning m-apo and o-apo replicas populated the m-state and occluded state, respectively (Table S5).

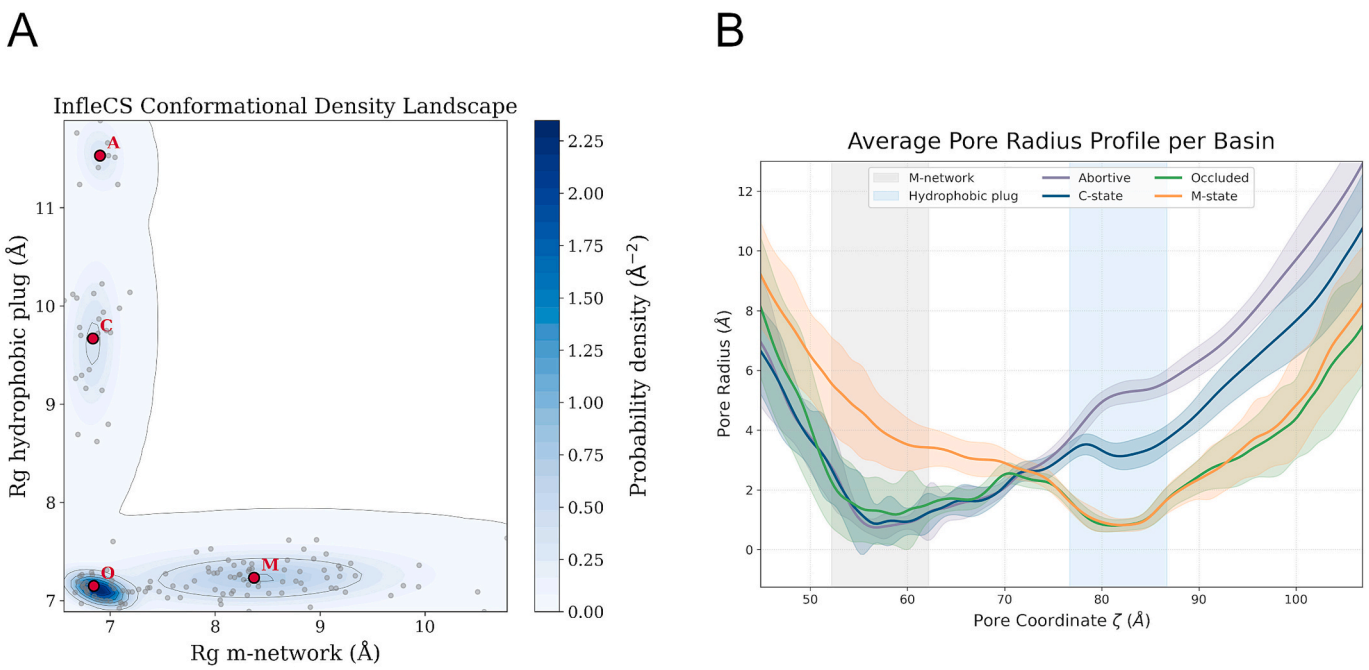

Fig. 5. (A) Conformational landscape from InfleCS density-based clustering, projected onto the mass-weighted radius of gyration of the m-network and of the hydrophobic plug. Colour represents the probability density ($Å^{-2}$) of the Gaussian mixture model evaluated directly from the fitted InfleCS model on 141 decorrelated frames (gray dots); this distribution reflects the probability density of unbiased sampling and should not be interpreted as an equilibrium free-energy surface. The four identified basins are labeled: A (abortive c-state), C (c-state), O (occluded), M (m-state). The higher density of the occluded basin reflects its narrower distribution in collective-variable space. (B) Average pore radius profile along the pore axis (ζ) for each of the four metastable states on 100 frames randomly sampled from each InfleCS basin. Solid lines represent the mean radius; shaded areas represent ± SD. Vertical bands indicate the approximate positions of the m-network (pink) and hydrophobic plug (blue).

As a further validation of the basins, the transitioning replicas are expected to spend part of their trajectory in the initial basin and part in the final one, if the classification is reliable. This is exactly the pattern observed: transitioning replicas show a mixed occupancy split between their initial and final states (Table S5 and Fig. S10), providing a geometric, reproducible counterpart to the structural convergence analyses of Section 3.2.1. It is important to point out again that this distribution reflects the probability density of unbiased sampling and should not be interpreted as an equilibrium free-energy landscape.

As an additional independent validation of the four basins, TM-align [13] was applied to 100 frames randomly sampled from each basin against the corresponding experimental structure, following the same approach used in Sections 3.1 and 3.2.1. Since no experimental structure is available for the occluded state, this comparison was restricted to the other basins.

Interestingly, the abortive c-state frames showed higher structural similarity to the inhibitor-bound crystal structure (PDB ID: 1OKC [8]) than the narrower c-state basin (TM-score 0.79 ± 0.01 *vs* 0.77 ± 0.01; RMSD 3.23 ± 0.14 *vs* 3.46 ± 0.14 Å; SD, $N = 100$), consistent with a resemblance to the more extreme, c-side opened configuration. This transient population likely reflects the initial relaxation of the predicted model, which subsequently converges toward a more compact conformation, in line with the expectation that the physiological c-state cavity is narrower than that of the inhibitor-bound structure [47].

The m-state basin showed comparable structural similarity to the fungal crystal structure (PDB ID: 6GCI [9]; TM-score 0.75 ± 0.02, RMSD 3.76 ± 0.23 Å, SD, N = 100), consistent with the good agreement already observed for the predicted model (Section 3.1).

Pore radius was also measured as a function of position along the pore axis (ζ) using the HOLE2 implementation [48] within the MDAnalysis library [49,50], on the same set of sampled frames (Fig. 5, Panel B). The abortive and c-state basins showed a pronounced minimum at the m-network region (0.75–0.87 Å, ζ ≈ 57 Å), while the m-state basin displayed a single minimum at the hydrophobic plug (0.81 Å, ζ ≈ 82 Å), with the m-network region open, as expected. The occluded basin showed constriction at both gates simultaneously (1.20 Å, ζ ≈ 57 Å; 0.82 Å, ζ ≈ 82 Å), consistent with an intermediate conformation along the transport cycle, in which the plug is already closed to an extent comparable to the m-state while the m-network remains constricted as well. This pattern provides a further structural confirmation of the four metastable states identified above.

3.2.3. *Distance-based classification of the conformational states*

To test whether the four populations identified by InfleCS are separated by genuine structural differences rather than by the specific choice of the two collective variables used to define them, a linear discriminant classifier (LDA) was trained on a large set of intraprotein distances selected by mutual information with the conformational state label. The classifier achieved near-perfect accuracy (99.7–100% across all tested feature-set sizes; Table S6) on held-out validation and test data, under a trajectory-level split designed to prevent leakage between temporally correlated frames. As a more stringent test, held-out transition frames not used during training were correctly assigned to the appropriate pair of adjacent states (abortive↔c-state, c-state↔occluded or occluded↔m-state) in 99.8% of cases, with no frame consistent with a direct, non-adjacent transition (*Supplementary Methods Section 3*). Because the classifier was trained on labels derived from InfleCS, this analysis does not validate the four states independently; rather, it shows that the InfleCS-defined populations remain well separated when described by a different set of features (intraprotein distances, rather than the Rg-based collective variables), consistent with the sequential abortive↔c-state↔occluded↔m-state ordering of the transitions characterized structurally in Section 3.2.1.

Finally, the distances that best discriminate each pair of adjacent basins were identified through pairwise discriminant analysis (Fig. 6, Tables S7-S9). The abortive↔c-state pair was dominated by distances

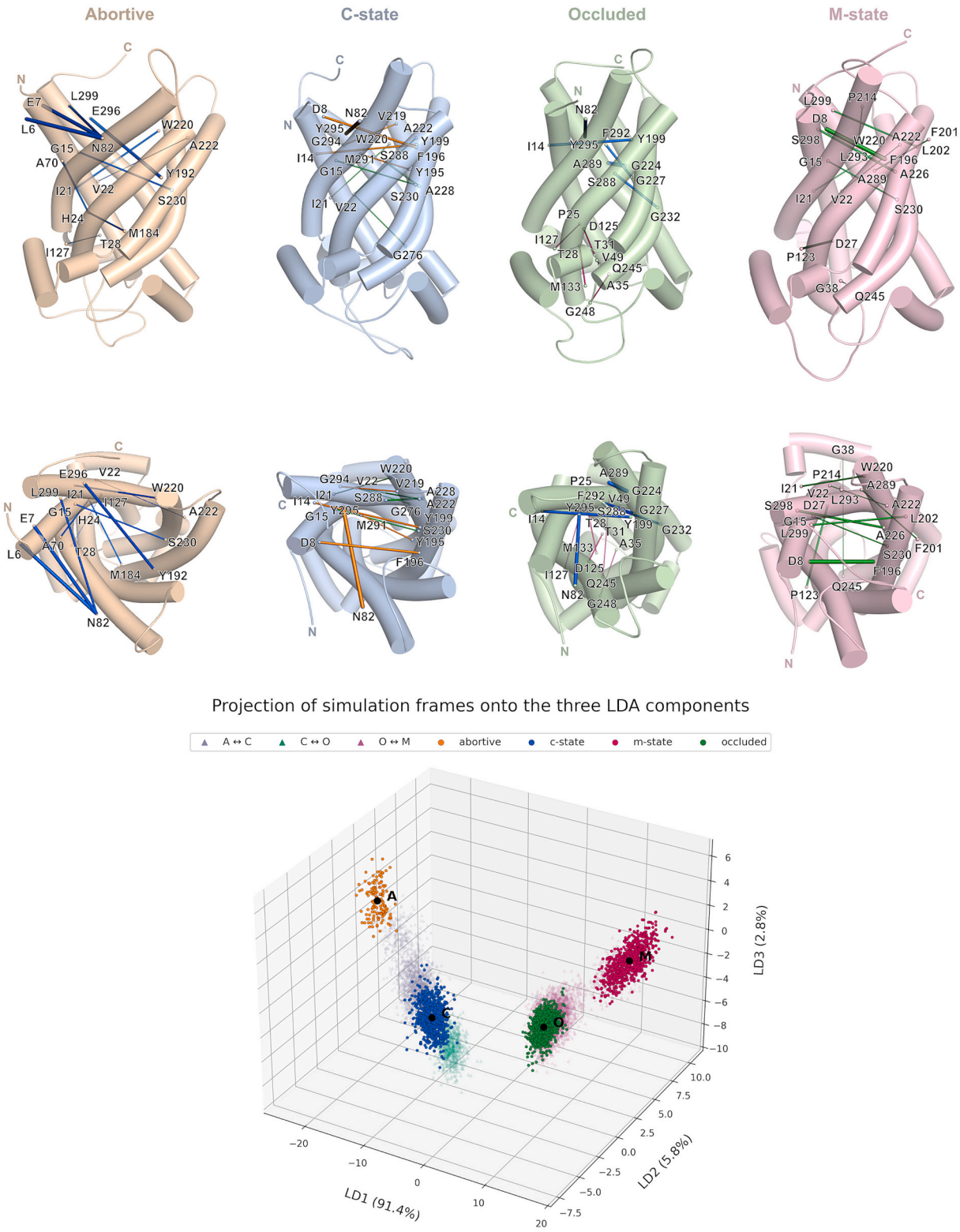

Fig. 6. Top row: cartoon tube representation of the front view of the four conformational states, from left to right, abortive, c-state, occluded, m-state. Middle row: IMS view of the same four states. The abortive is colored in orange, c-state in blue, occluded in green and m-state in pink. For the abortive and m-state, the top ten discriminant distances by contribution are shown; for c-state and occluded, which each border two adjacent states, the top five distances contributing to each of the two flanking transitions are shown (ten total). Distances are shown as pseudobonds connecting Cβ atoms (Cα for glycine), colored according to the state they point toward: *e.g.*, distances contributing to the c-state→abortive transition are colored orange (abortive), while distances contributing to the abortive→c-state transition are colored blue (c-state). Pseudobond thickness is proportional to each distance's contribution to the discriminant axis (*Supplementary Methods Section 3*). Bottom row: three-dimensional projection of the 50-feature LDA model onto its three discriminant axes (LD1–LD3, percentage of explained variance in parentheses). Training frames are colored by conformational state (same colour scheme as above); black circles mark the class centroids, labeled with the corresponding state initial (A, C, O, M). Triangles show held-out transition frames (*Supplementary Methods Section 3*), colored by the adjacent-state pair they were assigned to.

involving the hydrophobic plug residues (*e.g.*, Asp8-Phe196, Ile14-Tyr199, Tyr195-Met291), consistent with the marked difference in plug Rg already described (Section 3.2.2). The c-state↔occluded pair primarily involved the H5-H6 interface (*e.g.*, Gly224-Ala289, Gly232-Ser288, Gly227-Phe292), alongside additional plug-proximal and H1-mediated contacts. The occluded↔m-state pair was instead clearly dominated by distances between H1 and H3/H5 (*e.g.*, Thr31-Asp125, Pro25-Ile127, Ala35-Gly248, Val49-Gln245), a first indication that Domain I plays a distinctive role in this half of the conformational cycle. Notably, Asp125, which is one of the charged residues of the m-network, ranks among the top contributors for the occluded↔m-state pair (rank 2 and 9, Table S9).

3.2.4. *Asymmetric rearrangement of domain I*

The prominence of H1 among the discriminant distances for the occluded↔m-state pair has been further examined through structural analyses of the transitions.

In all the o-to-m transitions the main structural rearrangements were observed on helices H1, h12, H2 (Domain I), which moved apart to allow the opening of the transporter toward the matrix side, while other helices underwent negligible adjustments. The reverse m-to-o transition sampled by *m-apo 1* showed the same asymmetry in mirror: Domain I underwent the largest conformational displacement, while the rest of the protein acted as a rigid scaffold.

This asymmetry is evident in the per-helix RMSD analysis shown in Fig. 7, which identifies H1, h12, H2 and H3 as the most dynamic elements in both o↔m directions, with the rest of the protein remaining stationary. Domain I showed comparable RMSD to the rest of the protein in stable, non-transitioning c- and occluded replicas (1.80 ± 0.03 Å *vs* 1.76 ± 0.03 Å, mean ± SEM, $N = 10$); this difference increased markedly in all five o-to-m transitioning replicas (2.23 ± 0.13 Å *vs* 1.83 ± 0.02 Å) and in the reverse m-to-o transition (3.17 Å *vs* 1.75 Å). *o-holo 2*, whose incomplete transition is discussed separately in Section 3.2.1, is included in neither group.

Notably, this asymmetry in helix deformation persists beyond the active transitions: in the "native" m-state replicas as well, Domain I showed higher RMSD values than the rest of the protein, consistent with a looser connection, which grants greater freedom of movement (2.18 ± 0.03 Å *vs* 1.81 ± 0.06 Å, $N = 4$). It is important to point out that, because here RMSD is calculated on each helix independently, this measure captures internal helical deformation rather than rigid-body displacement relative to the rest of the protein; the latter is instead addressed directly by the analyses described below.

To test whether the asymmetric pattern of helical distortion observed in the heatmap of Fig. 7 corresponds to genuine rigid-body movement of specific helices or domains, several complementary analyses were performed.

First, the behavior of the m-network's charged couples was monitored throughout the simulations (Fig. S11). The Asp125-Lys241 (H3-H5) interaction was maintained in all simulations (3.52 ± 0.03 Å, mean ± SEM, $N = 21$); whereas Asp238-Lys30 (H5-H1) exhibited the largest increase in distance in o-to-m replicas, from 3.99 ± 0.46 Å to 11.47 ± 1.30 Å after the transition, consistent with the larger displacement of Domain I. Accordingly, the reverse m-to-o transition (*m-apo 1*) showed the opposite trend, going from 9.55 Å to 3.08 Å upon closure of the matrix side.

Additionally, inter-residue distances on H1 relative to the other odd-numbered helices (Thr31-Ile129, H1-H3; Ala35-Ala246, H1-H5; Fig. S12) demonstrated that H1 consistently showed the largest displacement relative to H5 across every transitioning simulation,

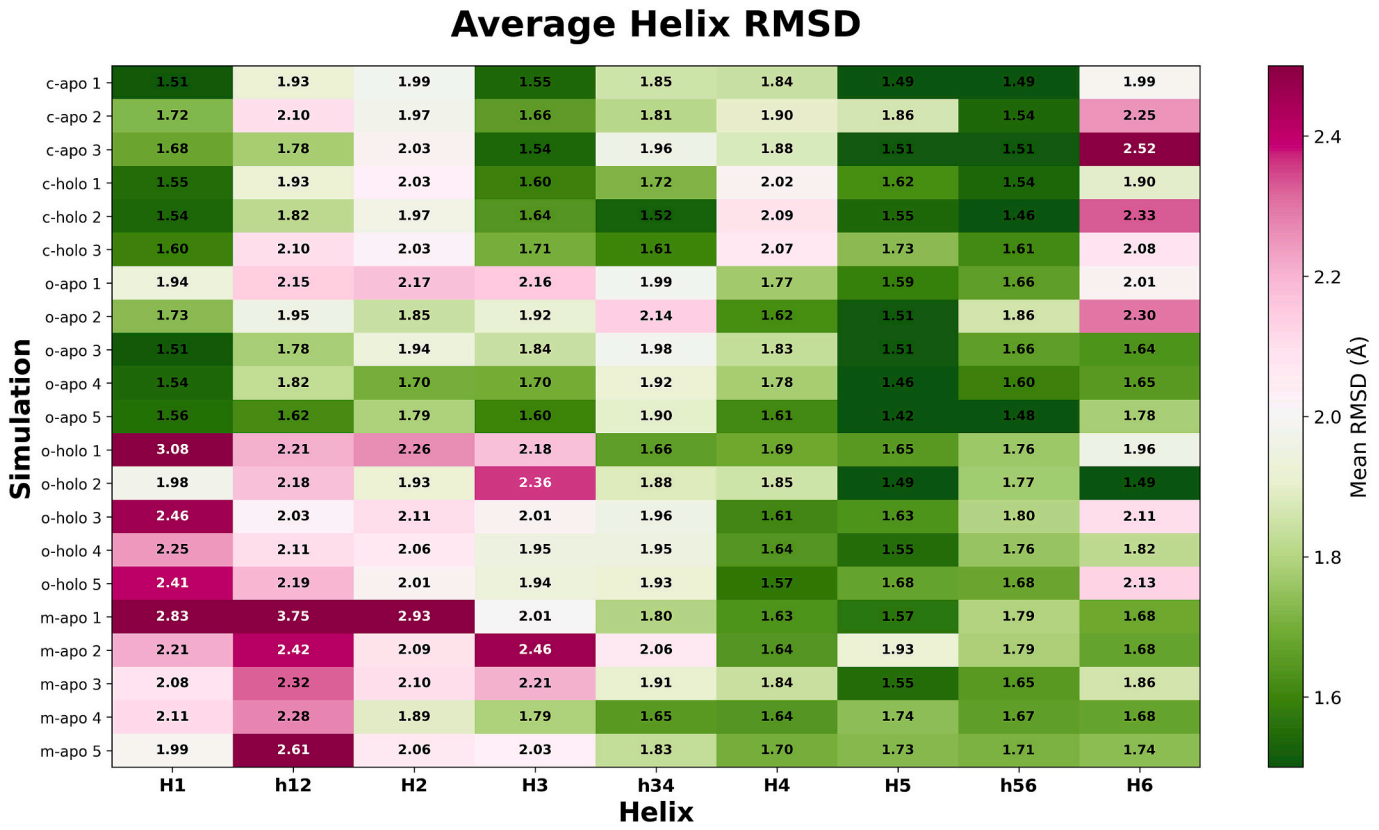

Fig. 7. Heatmap of the average per-helix RMSD value for each simulated system. Helices displaying lower RMSD values are shown in green, indicating smaller deviations from their initial positions, whereas helices with higher RMSD values are shown in fuchsia, reflecting larger structural fluctuations during the simulations. The elevated RMSD of H6 in c-state trajectories reflects its terminal position and greater conformational freedom in the IMS-open conformation, rather than a functional rearrangement.

increasing by 13.4 ± 1.5 Å; nearly twice the increase observed for H1-H3 (8.4 ± 1.3 Å, $N = 5$).

As a control, both distances remained stable in non-transitioning replicas (H1-H5: 4.22 ± 0.13 Å; H1-H3: 4.28 ± 0.07 Å, N = 5); while in transitioning ones the H1-H5 distance went from 4.44 ± 0.34 Å to 17.88 ± 1.47 Å and H1-H3 went from 4.52 ± 0.10 Å to 12.91 ± 1.30 Å. Notably, these helix distances ultimately reached values comparable to those of the native m-state replicas (H1-H5: 16.54 ± 1.31 Å; H1-H3:

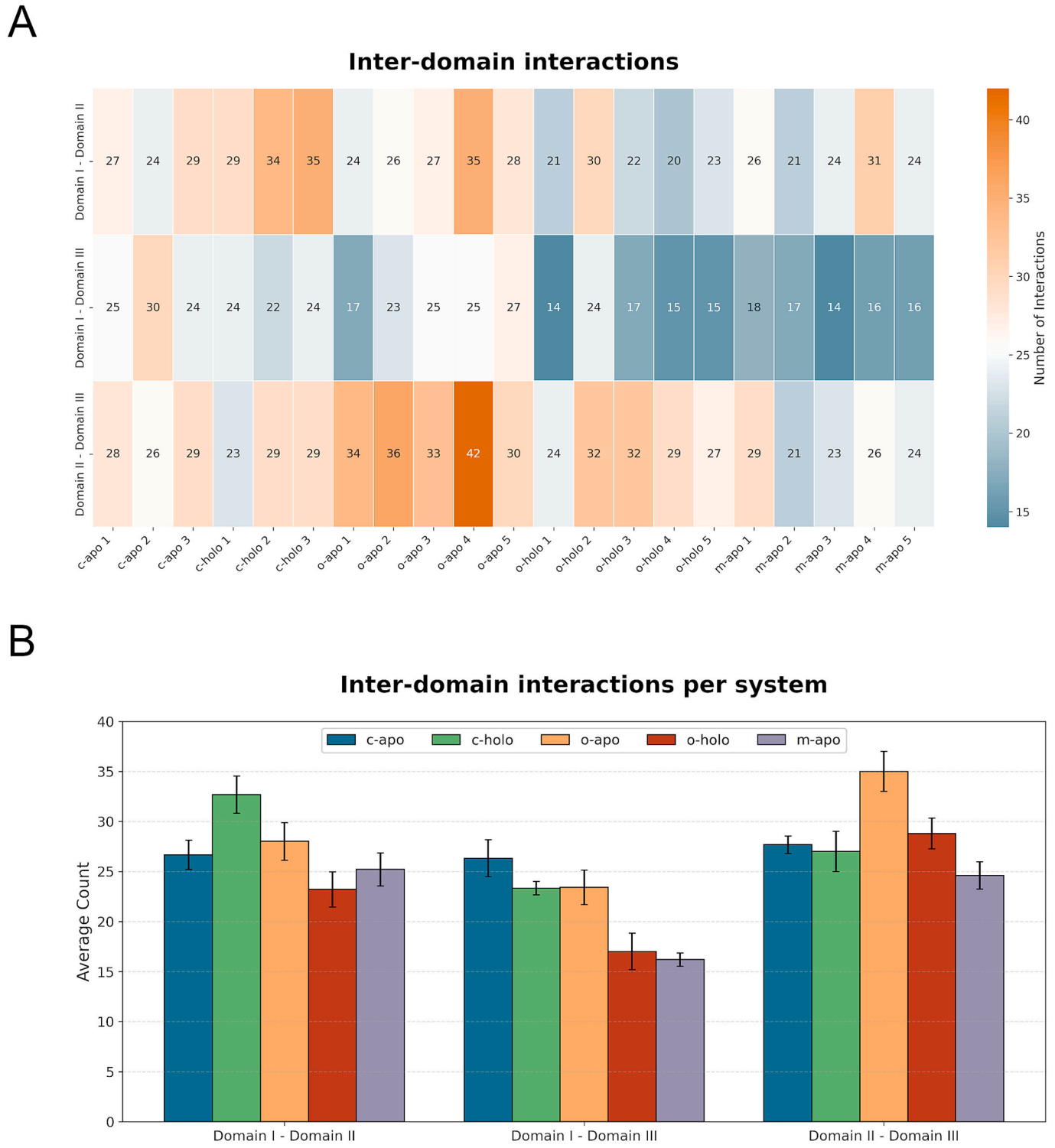

Fig. 8. Analysis of the intraprotein interactions. (A) Heatmap showing the total number of intraprotein contacts, including hydrogen bonds, salt bridges, and hydrophobic interactions, between inter-domain pairs (Domain I-II, I-III, II-III) for all 21 MD simulations. (B) Bar plots of average inter-domain contacts per system, with the three domain pairs displayed separately on the x-axis. Domain I-Domain III interactions are substantially reduced in m-apo and o-holo simulations, consistent with detachment of Domain I relative to the other domains. Error bars represent the standard error of the mean (SEM) across replicas, grouped by starting system ($N = 3$ for c-apo and c-holo; $N = 5$ for occluded-apo, occluded-holo and m-apo); each group includes both stable and transitioning replicas, as detailed in the main text.

11.57 ± 0.96 Å, $N = 4$).

Conversely, *m-apo 1* showed the opposite trend, with a progressive decrease, from 12.46 to 4.87 Å for the H1-H5 distance and 9.86 to 4.09 Å for the H1-H3, converging toward distance values comparable to those of the stable occluded replicas.

The detachment of Domain I is further supported by intraprotein contact analysis. The heatmap in Fig. 8 (Panel A) shows that in native m-state trajectories, as well as in simulations transitioning toward the m-state, Domain I engages in fewer interactions, particularly with Domain III. Average inter-domain contacts, represented as bar plots in the same figure (Panel B), quantify this reduction per system: Domain I-Domain III contacts averaged 26.3 ± 1.9, 23.3 ± 0.7 and 23.4 ± 1.7 (mean ± SEM) in the c-apo, c-holo and o-apo replicas (the latter including *o-apo 1*, the only transitioning replica in that group); decreasing to 17.0 ± 1.8 in o-holo and 16.2 ± 0.7 in the native m-state, supporting the asymmetric displacement of Domain I relative to the rest of the protein.

Interestingly, this behavior is consistent with observations across other mitochondrial carriers. Previous structural superimpositions and helix bending analyses on predicted models of the carnitine/acylcarnitine carrier (CAC, SLC25A20) [51] revealed that H1, H2 and partially H6 undergo the largest rearrangements and exhibit the highest variability in atomic contacts between the c- and m-state conformations, while the rest of the protein remains relatively compact.

Recent all-atom MD simulations of AAC by Li and colleagues [52] similarly highlighted a stable matrix-side core formed by Domains II and III, while Domain I remained more loosely connected. This asymmetric organization was already apparent in the crystallographic m-state structure of AAC (PDB ID: 6GCI [9]) but their simulation analyses suggested that this asymmetry is an intrinsic property of the carrier rather than a distortion induced by inhibitor binding [52]. An analogous asymmetric arrangement has been observed in a respiratory supercomplex from *Tetrahymena thermophila* (PDB ID: 7W5Z), where the structure of a mitochondrial carrier dimer (SLC25A11) was resolved by cryo-EM [53]. In this assembly, one of the monomers adopts a matrix-open conformation in which its Domain I is considerably more loosely associated with the rest of the protein.

Taken together, these observations across different members of the SLC25 family point to an asymmetric mechanism of conformational change that the present simulations of SLC25A48 captured directly.

3.2.5. The M2 loop as a structural correlate of the conformational transitions

Interestingly, the distance with the highest discriminant importance for the o↔m pair was Thr28-Met133 (Section 3.2.3; Table S9), involving a residue on H1 and the first residue of the M2 loop (residues 133–159), the matrix loop connecting H3 and h34 within Domain II.

To assess whether this loop adopted preferential positions, trajectories were clustered by its RMSD. In the most populated clusters of the c-state and stably occluded conformations, the loop was positioned below the cavity, oriented toward the space between h12 and h56, effectively closing the protein from the matrix side (Fig. S13). The M2 loop formed extensive intraprotein contacts in both the c- and occluded conformations, likely contributing to the structural stabilization of the matrix-closed side. In the o-apo systems, the loop established the most extensive interactions with H5 and with the M3 loop (Fig. S14).

By contrast, in trajectories converging toward the m-state, the loop adopted an extended conformation, distant from the cavity. Notably, during the *o-holo 1* simulation the M2 loop underwent a markedly different arrangement, establishing contacts with the bilayer membrane (Fig. S26). This peculiar behavior has been discussed in the *Supplementary Results and Discussion Section 1*.

These loop positions and motions were independently confirmed by Principal Component Analysis (PCA) of the trajectories, which identified the first principal component (PC1, Table S10) as predominantly associated with the M2 loop or with the disordered C-terminal IMS region of H6. The porcupine plots showing this pattern for all systems are reported in Fig. S15. In the c-state and stably occluded replicas, vectors direction along PC1 pointed toward the closing, capping-like configuration of the loop described above. In trajectories converging toward the m-state, vectors pointed outward, consistent with an opening-oriented conformation. Interestingly, during the m-to-o transition of *m-apo 1*, the loop moved inward, closing the cavity from below, effectively reaching positions like those observed in the c- and occluded systems.

Sequence comparison with other SLC25 carriers transporting similar substrates shows that SLC25A15 (ornithine carrier), SLC25A20 (CAC) and SLC25A29 (lysine and arginine carrier) lack a long loop in this region, while SLC25A45 (recently identified as a trimethyllysine and dimethylarginine carrier [54,55]) contains a loop of comparable length but with a different, proline-rich composition. These observations suggest that the M2 loop in SLC25A48 may play a specific regulatory and/or mechanical role during conformational transitions, although direct evidence is currently lacking.

3.3. Ligands and lipids

Beyond the conformational transitions and the structural asymmetry described above, neither the behavior of the ligand nor the response of the surrounding membrane has yet been addressed. First, none of the observed transitions were accompanied by membrane destabilization: quantitative analysis of the bilayer geometry showed only minor, localized deformations consistent with normal thermal fluctuations, with no persistent global bending detected across any system (Supplementary Figs. S16-S23).

The following paragraphs of this section examine in detail how the transporter engages its substrate and the surrounding lipids, in both the occluded and the c-state holo replicas.

In the case of o-to-m transitions, despite full opening of the internal cavity and water penetration, choline remained stably bound throughout the holo simulations. The conformational transitions observed therefore correspond to the opening step of the transport cycle, without a coupled substrate-release event, likely to happen during longer timescales. Ligand stability was ensured by a persistent aromatic cage formed by Tyr192, Tyr195 and Trp231, which enclosed the trimethylammonium group of choline through highly persistent cation-π interactions (mean persistence ± SEM: 99.4 ± 0.3%, 92.0 ± 2.4% and 99.3 ± 0.2% across the five replicas), complemented by a hydrogen bond with Asp188 (46.6 ± 4.1%) (Table S11, Fig. 9).

As already noted, across all c-state simulations the protein structure remained stable throughout, with only limited local fluctuations, although lipids played a relevant role. In detail, during *c-holo 1* choline remained stably bound to the same aromatic cage described above, while a lipid got inserted at the H1-H2 interface without perturbing ligand occupancy. In *c-holo 2* and *c-holo 3*, by contrast, simultaneous lipid insertion at both the H1-H2 and H5-H6 interfaces coincided with transient or complete displacement of choline toward a secondary site, near Phe77 and Tyr295, before re-entry and stabilization at the aromatic cage in the case of *c-holo 3* (Table S11 and S12, Fig. S24).

In the apo replicas, membrane lipids transiently approached the internal cavity at the same two interfaces, with the extent of penetration governed by the compactness of the surrounding helices (Table S13). In *c-apo 1*, whose more open starting conformation is reflected in the abortive sub-population described in Section 3.2.2, lipids reached more deeply into the cavity through H5-H6, interacting with several residues involved in ligand binding, whereas the more compact arrangement of *c-apo 2* and *c-apo 3* excluded lipids from this region, restricting insertion to the shallower H1-H2 interface. Notably, lipids occasionally engaged this same secondary site (Phe77 and Tyr295), mirroring the ligand itself. Representative frames illustrating lipid position and orientation across all six c-state replicas are shown in the Supplementary Figs. S24 and S25. This recurring transit through Phe77 and Tyr295 suggests it may function as an early binding site, sampled prior to full engagement of the ligand in the binding pocket, consistent with a multi-step binding

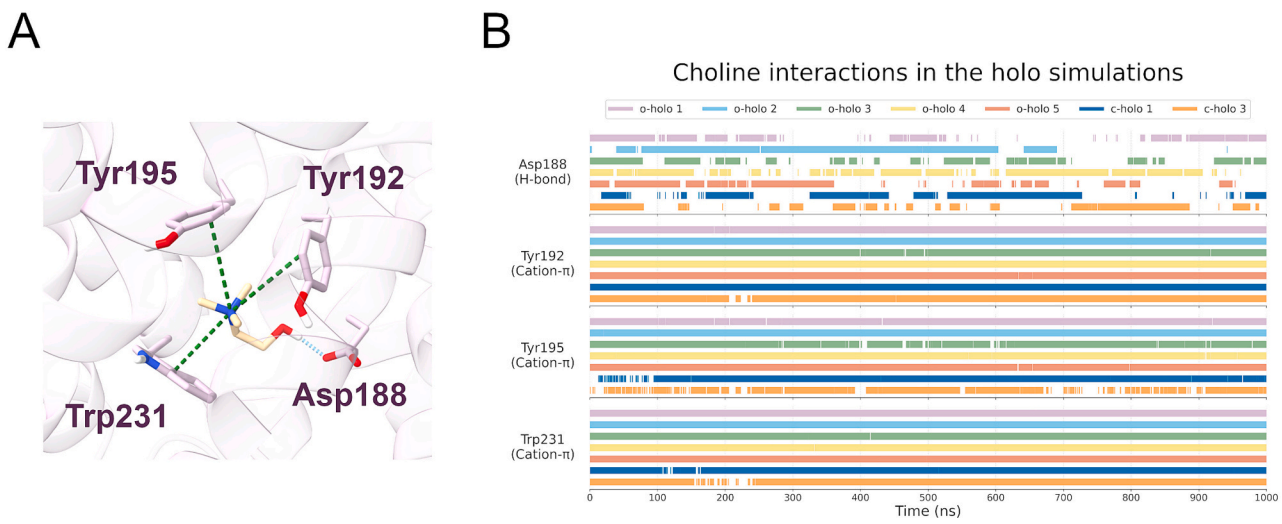

Fig. 9. Interactions between choline and SLC25A48 during the holo simulations. (A) Representative snapshot from the first replica of the o-holo system. The protein is represented as ribbons in orchid, while the interacting residues are shown as sticks; choline is represented as sticks, colored in beige. Hydrogen bonds are shown as light blue dashed lines and cation-π interactions as green dashed lines. Only polar hydrogens are shown for clarity. (B) Eventplot showing the time series of the interactions between choline and the protein residues of the aromatic cage. The graph displays the frames in which each interaction was observed during the MD simulations of the o- and c-holo simulations. *c-holo 2* has not been included given that choline, as described in the text, exits the cavity. For hydrogen bonds, interactions were counted only when the distance between the heavy atoms was within 3.4 Å, while for cation-π interactions the threshold was set to 6 Å.

mechanism already proposed for this protein family [7,51,56,57]. Notably, the corresponding residues in CAC (Phe90 and Phe287) were previously shown to engage the trimethylammonium group of propionylcarnitine in an analogous early-binding role [51], suggesting that this site may be conserved among SLC25 carriers transporting similar substrates.

Taken together, these observations indicate that lipid-protein interactions in the c-state are context-dependent rather than random and may contribute to stabilizing specific conformations depending on substrate occupancy, pointing to a possible coupling between the conformational dynamics of SLC25A48 and its membrane environment that merits further investigation.

4. Conclusions

The present work provides a comprehensive analysis of the conformational dynamics of the mitochondrial choline carrier SLC25A48, combining structure prediction with microsecond-scale MD simulations in a realistic mitochondrial membrane environment.

Unbiased simulations captured spontaneous transitions in both directions between the occluded and m-state and this bidirectional behavior was confirmed by structural convergence analyses and TM-align comparison to available crystal structures, and the four resulting conformational states were shown to remain well separated when described by a distinct set of features using a supervised classifier. Together, these results suggest that the occluded conformation acts as a kinetically accessible intermediate within the transport cycle, rather than an artifact of the predicted starting structures.

This is one of the very few cases [58] in which conformational transitions in a SLC25 carrier have been observed by classical MD on a sub-microsecond timescale without any applied bias. The sub-microsecond timescale on which the transitions are sampled deserves further consideration, since spontaneous conformational changes of secondary active transporters initiated from fully stable ground states typically require tens to hundreds of microseconds of aggregate sampling. For example, Latorraca et al. observed a transition to the inward-open state every 14 μs for the semiSWEET transporter [59], ~300 μs were required to reconstruct the complete transport cycle of the MFS transporter NarK from crystallographic endpoints [60] and a cumulative 64 μs to observe spontaneous transitions in the bacterial sodium-proton antiporter NhaA [40]. These timescales, however, reflect the stochastic waiting time for barrier crossing from a deep energy well, rather than the duration of the conformational change itself. Indeed, in Latorraca et al. the outward-open to occluded transition begins only after approximately 600 ns, whereas replicas initialized directly from the occluded state are substantially faster: 8 out of 14 reached the inward-open state within trajectories of 0.62–1.49 μs, so that the occluded-to-inward transition necessarily occurred during these timescales, markedly shorter than transitions starting from a fully stable ground state. By initializing the systems from the occluded intermediate, the long dwell time associated with the ground state is likely bypassed, placing the protein in a region of conformational space from which the transition toward the m-state is kinetically accessible. A directly relevant precedent is provided by Ohnuki and Okazaki [61], who used AF2-predicted intermediate conformations of NarK as starting points for MD simulations and observed large structural changes within the first 10 ns, with the complete transition to an inward-open-like conformation within 250 ns, *versus* the ~300 μs of aggregate sampling required from the crystallographic ground states [60].

A consistent picture emerges from a recent free-energy study of AAC [62], in which committor analysis identified the occluded state as a decisive kinetic checkpoint of inward transport: once this intermediate is reached, progression toward the matrix-open conformation becomes dominant. The transitions captured here for SLC25A48, initiated directly from the occluded intermediate, are therefore consistent with this broader kinetic picture.

A central outcome of this study is the identification of a pronounced, asymmetric conformational rearrangement underlying the o↔m transitions. Structural rearrangements predominantly involved Domain I (H1, h12 and H2), together with H3, while the remaining helices behaved as a comparatively rigid scaffold. This asymmetry was shown consistently by per-helix RMSD, inter-helical distances, m-network salt-bridge behavior and inter-domain contact analysis. A supervised classifier, trained without any knowledge of the transition trajectories, identified a set of intraprotein distances involving Domain I as the strongest discriminant between conformational states, further highlighting the asymmetry. LDA and PCA analysis of the MD simulations highlighted also a pronounced flexibility of the M2 loop, which seems to stabilize the matrix side closure in c- and occluded states. The presence of cancer-associated variants affecting residues of this loop (Arg139Trp

and Pro152His) further highlights its potential functional relevance and motivates future experimental investigation [63,64].

During the holo simulations, choline remained stably coordinated by a conserved aromatic cage (Tyr192, Tyr195, Trp231), even throughout the o-to-m transitions; while a transient early interaction site (Phe77 and Tyr295) was repeatedly sampled by both choline and membrane lipids in the c-state simulations, consistent with a multi-step binding mechanism analogous to that proposed for CAC [51].

A limitation of this study concerns the absence of an experimental structure for the occluded state of any SLC25 family member, which precludes direct validation of the predicted occluded conformations. While convergence across architecturally distinct prediction methods (Section 3.1) offers reassurance, it cannot fully exclude shared biases inherited from overlapping training data or structural homologs. Minor local inaccuracies in the starting models therefore cannot be excluded and will require experimental confirmation.

Finally, the complete transport cycle was not sampled within the present timescales: the transitions captured here correspond specifically to the opening step of the cycle; the c-to-o and o-to-c transitions, as well as substrate release, remain to be characterized. Furthermore, the intermediate behavior observed in *o-holo 2* (Section 3.2.1) suggests the existence of additional, partially occluded states along the transition pathway.

Future work should extend the conformational coverage of SLC25A48 through additional and longer trajectories, targeting these missing steps, to reconstruct the full transport cycle. The distinct residue pairs discriminating adjacent states, identified here through pairwise discriminant analysis, constitute a compact set of candidate collective variables for future enhanced-sampling studies. Such studies would aim at a converged, quantitative description of the transition free-energy surface. These directions represent natural extensions of the present study and will build upon the mechanistic insights already obtained from the MD simulations presented here.

CRediT authorship contribution statement

Virginia Quadrotta: Writing – review & editing, Writing – original draft, Methodology, Investigation, Formal analysis, Data curation, Conceptualization. **Beatrice Gasperini:** Writing – review & editing, Investigation, Formal analysis, Conceptualization. **Andrea Pasquadibisceglie:** Writing – review & editing, Supervision, Methodology, Investigation, Formal analysis, Conceptualization. **Fabio Polticelli:** Writing – review & editing, Supervision, Resources, Project administration, Investigation, Funding acquisition, Conceptualization.

Funding

This research was financed by the MUR-Italy Grants of Departments of Excellence—L. 232/2016—art.1 cc. 314–337 awarded to the Department of Science of Roma Tre University (2023–2027). Financial support by Project ECS 0000024 Rome Technopole, – NRP Mission 4 Component 2 Investment 1.5, Funded by the European Union - NextGenerationEU is also gratefully acknowledged.

The funding sources had no relation to the study design, collection, analysis and interpretation of data, writing of the report and decision to submit the article for publication.

Declaration of competing interest

The authors declare that they have no known competing financial interests or personal relationships that could have influenced the work reported in this paper.

Appendix A. Supplementary data

Supplementary data to this article can be found online at https://doi.org/10.1016/j.ijbiomac.2026.154090.

Data availability

The data that support the findings of this study are openly available in Zenodo at https://doi.org/10.5281/zenodo.21721870

References

[1] J.J. Ruprecht, E.R.S. Kunji, The SLC25 mitochondrial carrier family: structure and mechanism, Trends Biochem. Sci. 45 (2020) 244–258, https://doi.org/10.1016/j.tibs.2019.11.001.
[2] A.R.P. Verkerke, X. Shi, M. Li, Y. Higuchi, T. Yamamuro, D. Katoh, H. Nishida, C. Auger, I. Abe, R.E. Gerszten, et al., SLC25A48 controls mitochondrial choline import and metabolism, Cell Metab. 36 (2024) 2156–2166.e9, https://doi.org/10.1016/j.cmet.2024.07.010.
[3] D.J. Bernard, F. Pangilinan, C. Mendina, T. Desporte, S.M. Wincovitch, D.J. Walsh, R.K. Porter, A.M. Molloy, B. Shane, L.C. Brody, SLC25A48 influences plasma levels of choline and localizes to the inner mitochondrial membrane, Mol. Genet. Metab. 143 (2024) 108518, https://doi.org/10.1016/j.ymgme.2024.108518.
[4] A. Khan, G. Unlu, P. Lin, Y. Liu, E. Kilic, T.C. Kenny, K. Birsoy, E.R. Gamazon, Metabolic gene function discovery platform GeneMAP identifies SLC25A48 as necessary for mitochondrial choline import, Nat. Genet. 56 (2024) 1614–1623, https://doi.org/10.1038/s41588-024-01827-2.
[5] S. Patil, O. Borisov, N. Scherer, C. Wirth, P. Schlosser, M. Wuttke, S. Ehret, L. Hannibal, K.-U. Eckardt, C. Hunte, et al., The membrane transporter SLC25A48 enables transport of choline into human mitochondria, Kidney Int. 107 (2025) 296–301, https://doi.org/10.1016/j.kint.2024.06.022.
[6] S.H. Zeisel, Choline: critical role during fetal development and dietary requirements in adults, Annu. Rev. Nutr. 26 (2006) 229–250, https://doi.org/10.1146/annurev.nutr.26.061505.111156.
[7] V. Mavridou, M.S. King, S. Tavoulari, J.J. Ruprecht, S.M. Palmer, E.R.S. Kunji, Substrate binding in the mitochondrial ADP/ATP carrier is a step-wise process guiding the structural changes in the transport cycle, Nat. Commun. 13 (2022) 3585, https://doi.org/10.1038/s41467-022-31366-5.
[8] E. Pebay-Peyroula, C. Dahout-Gonzalez, R. Kahn, V. Trézéguet, G.J.-M. Lauquin, G. Brandolin, Structure of mitochondrial ADP/ATP carrier in complex with Carboxyatractyloside, Nature 426 (2003) 39–44, https://doi.org/10.1038/nature02056.
[9] J.J. Ruprecht, M.S. King, T. Zögg, A.A. Aleksandrova, E. Pardon, P.G. Crichton, J. Steyaert, E.R.S. Kunji, The molecular mechanism of transport by the mitochondrial ADP/ATP carrier, Cell 176 (2019) 435–447.e15, https://doi.org/10.1016/j.cell.2018.11.025.
[10] The UniProt Consortium, UniProt: the universal protein knowledgebase in 2023, Nucleic Acids Res. 51 (2023) D523–D531, https://doi.org/10.1093/nar/gkac1052.
[11] J. Abramson, J. Adler, J. Dunger, R. Evans, T. Green, A. Pritzel, O. Ronneberger, L. Willmore, A.J. Ballard, J. Bambrick, et al., Accurate structure prediction of biomolecular interactions with AlphaFold 3, Nature 630 (2024) 493–500, https://doi.org/10.1038/s41586-024-07487-w.
[12] M. Mirdita, K. Schütze, Y. Moriwaki, L. Heo, S. Ovchinnikov, M. Steinegger, ColabFold: making protein folding accessible to all, Nat. Methods 19 (2022) 679–682, https://doi.org/10.1038/s41592-022-01488-1.
[13] Y. Zhang, J. Skolnick, TM-align: a protein structure alignment algorithm based on the TM-score, Nucleic Acids Res. 33 (2005) 2302–2309, https://doi.org/10.1093/nar/gki524.
[14] J. Wohlwend, G. Corso, S. Passaro, N. Getz, M. Reveiz, K. Leidal, W. Swiderski, L. Atkinson, T. Portnoi, I. Chinn, et al., Boltz-1 democratizing biomolecular interaction modeling, bioRxiv (2025), https://doi.org/10.1101/2024.11.19.624167, 2024.11.19.624167.
[15] B.R. Brooks, C.L. Brooks III, A.D. Mackerell Jr., L. Nilsson, R.J. Petrella, B. Roux, Y. Won, G. Archontis, C. Bartels, S. Boresch, et al., CHARMM: the biomolecular simulation program, J. Comput. Chem. 30 (2009) 1545–1614, https://doi.org/10.1002/jcc.21287.
[16] S. Jo, T. Kim, V.G. Iyer, W. Im, CHARMM-GUI: a web-based graphical user Interface for CHARMM, J. Comput. Chem. 29 (2008) 1859–1865, https://doi.org/10.1002/jcc.20945.
[17] J. Lee, X. Cheng, J.M. Swails, M.S. Yeom, P.K. Eastman, J.A. Lemkul, S. Wei, J. Buckner, J.C. Jeong, Y. Qi, et al., CHARMM-GUI input generator for NAMD, GROMACS, AMBER, OpenMM, and CHARMM/OpenMM simulations using the CHARMM36 additive force field, J. Chem. Theory Comput. 12 (2016) 405–413, https://doi.org/10.1021/acs.jctc.5b00935.
[18] I.D. Pogozheva, G.A. Armstrong, L. Kong, T.J. Hartnagel, C.A. Carpino, S.E. Gee, D. M. Picarello, A.S. Rubin, J. Lee, S. Park, et al., Comparative molecular dynamics simulation studies of realistic eukaryotic, prokaryotic, and archaeal membranes, J. Chem. Inf. Model. 62 (2022) 1036–1051, https://doi.org/10.1021/acs.jcim.1c01514.
[19] J. Huang, S. Rauscher, G. Nawrocki, T. Ran, M. Feig, B.L. de Groot, H. Grubmüller, A.D. MacKerell, CHARMM36m: an improved force field for folded and intrinsically disordered proteins, Nat. Methods 14 (2017) 71–73, https://doi.org/10.1038/nmeth.4067.
[20] D.A. Case, H.M. Aktulga, K. Belfon, I.Y. Ben-Shalom, J.T. Berryman, S.R. Brozell, D. S. Cerutti, T.E. Cheatham III, G.A. Cisneros, V.W.D. Cruzeiro, T.A. Darden, N. Forouzesh, M. Ghazimirsaeed, G. Giambaşu, T. Giese, M.K. Gilson, H. Gohlke, A.

W. Goetz, J. Harris, Z. Huang, S. Izadi, S.A. Izmailov, K. Kasavajhala, M.C. Kaymak, A. Kovalenko, T. Kurtzman, T.S. Lee, P. Li, Z. Li, C. Lin, J. Liu, T. Luchko, R. Luo, M. Machado, M. Manathunga, K.M. Merz, Y. Miao, O. Mikhailovskii, G. Monard, H. Nguyen, K.A. O'Hearn, A. Onufriev, F. Pan, S. Pantano, A. Rahnamoun, D. R. Roe, A. Roitberg, C. Sagui, S. Schott-Verdugo, A. Shajan, J. Shen, C. L. Simmerling, N.R. Skrynnikov, J. Smith, J. Swails, R.C. Walker, J. Wang, J. Wang, X. Wu, Y. Wu, Y. Xiong, Y. Xue, D.M. York, C. Zhao, Q. Zhu, P.A. Kollman, Amber 2024, University of California, San Francisco, 2024.

[21] K.-H. Chow, D.M. Ferguson, Isothermal-isobaric molecular dynamics simulations with Monte Carlo volume sampling, Comput. Phys. Commun. 91 (1995) 283–289, https://doi.org/10.1016/0010-4655(95)00059-O.

[22] T. Darden, D. York, L. Pedersen, Particle mesh Ewald: an N·log(N) method for Ewald sums in large systems, J. Chem. Phys. 98 (1993) 10089–10092, https://doi.org/10.1063/1.464397.

[23] D.R. Koes, M.P. Baumgartner, C.J. Camacho, Lessons learned in empirical scoring with Smina from the CSAR 2011 benchmarking exercise, J. Chem. Inf. Model. 53 (2013) 1893–1904, https://doi.org/10.1021/ci300604z.

[24] A.T. McNutt, P. Francoeur, R. Aggarwal, T. Masuda, R. Meli, M. Ragoza, J. Sunseri, D.R. Koes, GNINA 1.0: molecular docking with deep learning, Aust. J. Chem. 13 (2021) 43, https://doi.org/10.1186/s13321-021-00522-2.

[25] T. Sterling, J.J. Irwin, ZINC 15 – ligand discovery for everyone, J. Chem. Inf. Model. 55 (2015) 2324–2337, https://doi.org/10.1021/acs.jcim.5b00559.

[26] E.C. Meng, T.D. Goddard, E.F. Pettersen, G.S. Couch, Z.J. Pearson, J.H. Morris, T. E. Ferrin, UCSF ChimeraX: tools for structure building and analysis, Protein Sci. 32 (2023) e4792, https://doi.org/10.1002/pro.4792.

[27] E.F. Pettersen, T.D. Goddard, C.C. Huang, G.S. Couch, D.M. Greenblatt, E.C. Meng, T.E. Ferrin, UCSF chimera—a visualization system for exploratory research and analysis, J. Comput. Chem. 25 (2004) 1605–1612, https://doi.org/10.1002/jcc.20084.

[28] A.M. Westerlund, L. Delemotte, InfleCS: clustering free energy landscapes with Gaussian mixtures, J. Chem. Theory Comput. 15 (2019) 6752–6759, https://doi.org/10.1021/acs.jctc.9b00454.

[29] Y. Kang, L. Chen, Structural basis for the binding of DNP and purine nucleotides onto UCP1, Nature 620 (2023) 226–231, https://doi.org/10.1038/s41586-023-06332-w.

[30] J. Jumper, R. Evans, A. Pritzel, T. Green, M. Figurnov, O. Ronneberger, K. Tunyasuvunakool, R. Bates, A. Žídek, A. Potapenko, et al., Highly accurate protein structure prediction with AlphaFold, Nature 596 (2021) 583–589, https://doi.org/10.1038/s41586-021-03819-2.

[31] M. Akdel, D.E.V. Pires, E.P. Pardo, J. Jänes, A.O. Zalevsky, B. Mészáros, P. Bryant, L.L. Good, R.A. Laskowski, G. Pozzati, et al., A structural biology community assessment of AlphaFold2 applications, Nat. Struct. Mol. Biol. 29 (2022) 1056–1067, https://doi.org/10.1038/s41594-022-00849-w.

[32] M. Varadi, S. Anyango, M. Deshpande, S. Nair, C. Natassia, G. Yordanova, D. Yuan, O. Stroe, G. Wood, A. Laydon, et al., AlphaFold protein structure database: massively expanding the structural coverage of protein-sequence space with high-accuracy models, Nucleic Acids Res. 50 (2021) D439–D444, https://doi.org/10.1093/nar/gkab1061.

[33] G. Kim, S. Lee, E. Levy Karin, H. Kim, Y. Moriwaki, S. Ovchinnikov, M. Steinegger, M. Mirdita, Easy and accurate protein structure prediction using ColabFold, Nat. Protoc. 20 (2025) 620–642, https://doi.org/10.1038/s41596-024-01060-5.

[34] D. del Alamo, D. Sala, H.S. Mchaourab, J. Meiler, Sampling alternative conformational states of transporters and receptors with AlphaFold2, eLife 11 (2022) e75751, https://doi.org/10.7554/eLife.75751.

[35] A. Pasquadibisceglie, A. Leccese, F. Polticelli, A computational study of the structure and function of human Zrt and Irt-like proteins metal transporters: an elevator-type transport mechanism predicted by AlphaFold2, Front. Chem. 10 (2022), https://doi.org/10.3389/fchem.2022.1004815.

[36] H.K. Wayment-Steele, A. Ojoawo, R. Otten, J.M. Apitz, W. Pitsawong, M. Hömberger, S. Ovchinnikov, L. Colwell, D. Kern, Predicting multiple conformations via sequence clustering and AlphaFold2, Nature 625 (2024) 832–839, https://doi.org/10.1038/s41586-023-06832-9.

[37] X. Guan, Q.-Y. Tang, W. Ren, M. Chen, W. Wang, P.G. Wolynes, W. Li, Predicting protein conformational motions using energetic frustration analysis and AlphaFold2, Proc. Natl. Acad. Sci. USA 121 (2024) e2410662121, https://doi.org/10.1073/pnas.2410662121.

[38] D.U. Ferreiro, E.A. Komives, P.G. Wolynes, Frustration, function and folding, Curr. Opin. Struct. Biol. 48 (2018) 68–73, https://doi.org/10.1016/j.sbi.2017.09.006.

[39] P. Bryant, F. Noé, Structure prediction of alternative protein conformations, Nat. Commun. 15 (2024) 7328, https://doi.org/10.1038/s41467-024-51507-2.

[40] T. Xie, J. He, S. Sun, Y. Chen, J. Huang, Y. Huang, Molecular mechanism of Na+/H + Antiporting in NhaA, J. Chem. Theory Comput. 21 (2025) 9107–9119, https://doi.org/10.1021/acs.jctc.5c00632.

[41] A.J. Robinson, C. Overy, E.R.S. Kunji, The mechanism of transport by mitochondrial carriers based on analysis of symmetry, Proc. Natl. Acad. Sci. 105 (2008) 17766–17771, https://doi.org/10.1073/pnas.0809580105.

[42] D.V. Miniero, F. Palmieri, V. Quadrotta, F. Polticelli, L. Palmieri, M. Monné, Functional roles of the charged residues of the C- and M-gates in the yeast mitochondrial NAD+ transporter Ndt1p, Int. J. Mol. Sci. 25 (2024) 13557, https://doi.org/10.3390/ijms252413557.

[43] H. Oheda, M. Inoue, T. Ekimoto, T. Yamane, M. Ikeguchi, Co-Folding of Membrane Proteins and Lipid Molecules Improves Membrane-Protein Structure Prediction Accuracy, 2026, 2026.03.24.713847.

[44] Z. Lin, H. Akin, R. Rao, B. Hie, Z. Zhu, W. Lu, N. Smetanin, R. Verkuil, O. Kabeli, Y. Shmueli, et al., Evolutionary-scale prediction of atomic-level protein structure with a language model, Science 379 (2023) 1123–1130, https://doi.org/10.1126/science.ade2574.

[45] E.M. Quistgaard, C. Löw, P. Moberg, L. Trésaugues, P. Nordlund, Structural basis for substrate transport in the GLUT-homology family of monosaccharide transporters, Nat. Struct. Mol. Biol. 20 (2013) 766–768, https://doi.org/10.1038/nsmb.2569.

[46] A. Pietropaolo, C.L. Pierri, F. Palmieri, M. Klingenberg, The switching mechanism of the mitochondrial ADP/ATP carrier explored by free-energy landscapes, Biochim. Biophys. Acta Bioenerg. 1857 (2016) 772–781, https://doi.org/10.1016/j.bbabio.2016.02.006.

[47] M. Klingenberg, The ADP and ATP transport in mitochondria and its carrier, Biochim. Biophys. Acta Biomembr. 1778 (2008) 1978–2021, https://doi.org/10.1016/j.bbamem.2008.04.011.

[48] O.S. Smart, J.G. Neduvelil, X. Wang, B.A. Wallace, M.S.P. Sansom, HOLE: a program for the analysis of the pore dimensions of Ion Channel structural models, J. Mol. Graph. 14 (1996) 354–360, https://doi.org/10.1016/S0263-7855(97)00009-X.

[49] R. Gowers, M. Linke, J. Barnoud, T. Reddy, M. Melo, S. Seyler, J. Domański, D. Dotson, S. Buchoux, I. Kenney, et al., MDAnalysis: A Python Package for the Rapid Analysis of Molecular Dynamics Simulations.; Austin, Texas, 2016, pp. 98–105.

[50] N. Michaud-Agrawal, E.J. Denning, T.B. Woolf, O. Beckstein, MDAnalysis: a toolkit for the analysis of molecular dynamics simulations, J. Comput. Chem. 32 (2011) 2319–2327, https://doi.org/10.1002/jcc.21787.

[51] A. Pasquadibisceglie, V. Quadrotta, F. Polticelli, In silico analysis of the structural dynamics and substrate recognition determinants of the human mitochondrial carnitine/Acylcarnitine SLC25A20 transporter, Int. J. Mol. Sci. 24 (2023) 3946, https://doi.org/10.3390/ijms24043946.

[52] Y. Li, Q. Yi, Y. Cai, Y. Zhang, J. Kong, P. Jiang, X. Cang, Structural dynamics of the mitochondrial ADP/ATP carrier support an asymmetric transport mechanism, Int. J. Biol. Macromol. (2025) 148348, https://doi.org/10.1016/j.ijbiomac.2025.148348.

[53] L. Zhou, M. Maldonado, A. Padavannil, F. Guo, J.A. Letts, Structures of Tetrahymena's respiratory chain reveal the diversity of eukaryotic Core metabolism, Science 376 (2022) 831–839, https://doi.org/10.1126/science.abn7747.

[54] M.M. Dias, M.S. King, E. Shokry, S. Lilla, N. Paul, P. Thomason, S. Zanivan, D. Sumpton, E.R.S. Kunji, T. MacVicar, SLC25A45 is required for mitochondrial uptake of methylated amino acids and de novo carnitine biosynthesis, Mol. Cell 85 (2025) 4093–4104.e8, https://doi.org/10.1016/j.molcel.2025.08.018.

[55] A. Khan, F.S. Yen, G. Unlu, N.L. DelGaudio, R. Erdal, M. Xiao, K. Wangdu, K. Cho, Eric.R. Gamazon, G.J. Patti, et al., Machine learning-guided discovery of SLC25A45 as a mediator of mitochondrial methylated amino acid import and carnitine synthesis, Cell Metab. 37 (2025) 2220–2232.e8, https://doi.org/10.1016/j.cmet.2025.09.015.

[56] S. Yao, Q. Yi, B. Ma, X. Mao, Y. Chen, M.-X. Guan, X. Cang, Mechanistic insights into multiple-step transport of mitochondrial ADP/ATP carrier, Comput. Struct. Biotechnol. J. 20 (2022) 1829–1840, https://doi.org/10.1016/j.csbj.2022.03.032.

[57] S. Aluvila, J. Sun, D.H.T. Harrison, D.E. Walters, R.S. Kaplan, Inhibitors of the mitochondrial citrate transport protein: validation of the role of substrate binding residues and discovery of the first purely competitive inhibitor, Mol. Pharmacol. 77 (2010) 26–34, https://doi.org/10.1124/mol.109.058750.

[58] M. Prejanò, A. Tonazzi, N. Giangregorio, C. Indiveri, T. Marino, Lanthanides Gd and Tm can inhibit carnitine/acylcarnitine transporter: insights from all-atoms simulations, ChemBioChem 26 (2025) e202401018, https://doi.org/10.1002/cbic.202401018.

[59] N.R. Latorraca, N.M. Fastman, A.J. Venkatakrishnan, W.B. Frommer, R.O. Dror, L. Feng, Mechanism of substrate translocation in an alternating access transporter, Cell 169 (2017) 96–107.e12, https://doi.org/10.1016/j.cell.2017.03.010.

[60] J. Feng, B. Selvam, D. Shukla, How do antiporters exchange substrates across the cell membrane? An atomic-level description of the complete exchange cycle in NarK, Structure 29 (2021) 922–933.e3, https://doi.org/10.1016/j.str.2021.03.014.

[61] J. Ohnuki, K. Okazaki, Integration of AlphaFold with molecular dynamics for efficient conformational sampling of transporter protein NarK, J. Phys. Chem. B 128 (2024) 7530–7537, https://doi.org/10.1021/acs.jpcb.4c02726.

[62] C. Tang, M.P. Pandey, C.G. Chen, A. Megías, F. Dehez, C. Chipot, Breaking the Timescale Barrier: Generative Discovery of Conformational Free-Energy Landscapes and Transition Pathways, 2025.

[63] R.K. Gopal, K. Kübler, S.E. Calvo, P. Polak, D. Livitz, D. Rosebrock, P.M. Sadow, B. Campbell, S.E. Donovan, S. Amin, et al., Widespread chromosomal losses and mitochondrial DNA alterations as genetic drivers in Hürthle cell carcinoma, Cancer Cell 34 (2018) 242–255.e5, https://doi.org/10.1016/j.ccell.2018.06.013.

[64] D.M. Muzny, M.N. Bainbridge, K. Chang, H.H. Dinh, J.A. Drummond, G. Fowler, C. L. Kovar, L.R. Lewis, M.B. Morgan, I.F. Newsham, et al., Comprehensive molecular characterization of human colon and rectal cancer, Nature 487 (2012) 330–337, https://doi.org/10.1038/nature11252.